

SPATIALLY-RESOLVED HST GRISM SPECTROSCOPY OF A LENSED EMISSION LINE GALAXY AT $Z \sim 1$

BRENDA L. FRYE^{2,3,4}, MAIREAD HURLEY⁵, DAVID V. BOWEN⁶, GERHARDT MEURER⁷, KEREN SHARON⁸, AMBER STRAUGHN⁹, DAN COE¹⁰, TOM BROADHURST¹¹ AND PURAGRA GUHATHAKURTA¹²

ACCEPTED TO APJ: May 11, 2012

ABSTRACT

We take advantage of gravitational lensing amplification by Abell 1689 ($z=0.187$) to undertake the first space-based census of emission line galaxies (ELGs) in the field of a massive lensing cluster. Forty-three ELGs are identified to a flux of $i_{775}=27.3$ via slitless grism spectroscopy. One ELG (at $z=0.7895$) is very bright owing to lensing magnification by a factor of ≈ 4.5 . Several Balmer emission lines detected from ground-based follow-up spectroscopy signal the onset of a major starburst for this low-mass galaxy ($M_* \approx 2 \times 10^9 M_\odot$) with a high specific star formation rate ($\approx 20 \text{ Gyr}^{-1}$). From the blue emission lines we measure a gas-phase oxygen abundance consistent with solar ($12+\log(\text{O}/\text{H})=8.8 \pm 0.2$). We break the continuous line-emitting region of this giant arc into seven $\sim 1\text{kpc}$ bins (intrinsic size) and measure a variety of metallicity dependent line ratios. A weak trend of increasing metal fraction is seen toward the dynamical center of the galaxy. Interestingly, the metal line ratios in a region offset from the center by $\sim 1\text{kpc}$ have a placement on the blue HII region excitation diagram with $f([\text{OIII}])/f(\text{H}\beta)$ and $f([\text{NeIII}])/f(\text{H}\beta)$ that can be fit by an AGN. This asymmetrical AGN-like behavior is interpreted as a product of shocks in the direction of the galaxy's extended tail, possibly instigated by a recent galaxy interaction.

Subject headings: cosmology: gravitational lensing – galaxies: clusters: general – galaxies: clusters: individual (A1689) – galaxies: distances and redshifts – galaxies: fundamental parameters

1. INTRODUCTION

Star formation in galaxies peaks at redshifts $z \sim 2$ (Reddy et al. 2005; Conzelmann et al. 2011), with an overall decline in the global star formation rate density towards later cosmic times (Lilly et al. 1996). Galaxies during the critical redshift range of $1 < z < 3$ are actively converting gas into stars and at least to some extent, building up central supermassive black holes (Reddy et al. 2008; Somerville 2009). Morphologically, these galaxies are already well underway with assuming the familiar shapes of the Hubble sequence (Kriek et al. 2009). Given the

unfortunate placement of major star formation features split between the optical and infrared passbands, building up a database of ELGs during this important cosmic epoch is slow.

Sample sizes of ELGs at these intermediate redshifts are small and comprise necessarily the brightest examples. Properties of these ELGs are determined typically from ratios of strong rest-frame optical emission lines. The values for the line ratios are persistently high compared to the standard excitation sequence for HII regions (Erb et al. 2006; Straughn et al. 2009; Pérez-Montero et al. 2009; Xia et al. 2011; Trump et al. 2011). In turn the elevated line ratios are generally accompanied by higher ionization parameters and electron densities, indicating that physical conditions may be different from the local universe (Liu et al. 2008; Brinchmann et al. 2008; Lehnert et al. 2009; Richard et al. 2011). Spatially-resolved observations can assist with the search for an explanation of these consistently high nebular line ratios. In one case of a field galaxy at $z = 1.6$ HDF-BMZ1299, integral field unit observations have revealed line ratios in the innermost $\sim 1.5 \text{ kpc}$ that are best-fit by an AGN. This measurement would not have been achievable in the spectrum integrated over the whole object (Wright et al. 2010). Similarly, a Hubble Space Telescope (HST) Wide Field Camera 3 (WFC3) grism study of ELGs from CANDLES (Goggin et al. 2011; Koekemoer et al. 2011) data in GOODS-S reveal the likelihood of weak AGN activity in $z \sim 2$ low mass, low metallicity galaxies (Trump et al. 2011).

It is feasible to use low resolution grism spectroscopy with HST ACS to study ELGs and also galaxies with strong breaks (bulges, Lyman-break galaxies). This approach has been used extensively by the Grism Advanced Camera Program for Extragalactic Science (GRAPES)

¹ Based, in part, on data obtained with the W. M. Keck Observatory, which is operated as a scientific partnership among the California Institute of Technology, the University of California, and NASA, and was made possible by the generous financial support of the W. M. Keck Foundation.

² Steward Observatory, Department of Astronomy, University of Arizona, 933 N. Cherry Avenue, Tucson, AZ 85721

³ Department of Physics and Astronomy, SUNY Stony Brook, Stony Brook, NY 11794-3800

⁴ Department of Physics & Astronomy, University of San Francisco, 2130 Fulton Street, San Francisco, CA 94117

⁵ School of Physical Sciences, Dublin City University, Glasnevin 9, Dublin, Ireland; mairead.hurley5@mail.dcu.ie

⁶ Department of Astrophysical Sciences, Peyton Hall, Princeton University, Princeton, NJ 08540

⁷ International Centre for Radio Astronomy Research, The University of Western Australia M468, 35 Stirling Highway, Crawley, WA 6009, Australia

⁸ Department of Astronomy and Astrophysics, The University of Chicago, Chicago, Illinois 60637

⁹ Astrophysics Science Division, Goddard Space Flight Center, Code 665, Greenbelt, MD 20771

¹⁰ Space Telescope Science Institute, 3700 San Martin Drive, Baltimore, MD 21218

¹¹ Ikerbasque, Basque Foundation for Science, 48011 Bilbao, Spain

¹² UCO/Lick Observatory, Department of Astronomy and Astrophysics, University of California, Santa Cruz, CA 95064

and Probing Evolution and Reionization Spectroscopically (PEARS) Treasury teams (PI: Malhotra). For example, Hathi et al. (2009) studied the stellar populations of late-type galaxies at $z \sim 1$ in the Hubble Ultra Deep Field (HUDF) using low resolution grism spectroscopy. They identified the bulges in a sample of 34 galaxies by a combination of their prominent 4000 Å break and visual morphologies. They measured stellar ages in the bulges that are similar to stellar ages in the inner disks and used this information to constrain galaxy formation mechanisms. Ferreras et al. (2009) measured galaxy properties for a sample of 228 galaxies at $z \sim 1$ selected by morphology and HST ACS grism spectroscopy to be early-types. They modeled the star formation histories and found the galaxy formation epoch to correlate strongly with stellar mass in massive early-type galaxies. Xia et al. (2011) reported on a comparison of 76 ELGs in Chandra Deep Field South (CDFS) acquired with both the ACS grism and ground-based spectrographs covering similar wavelengths. They compared the grism redshift estimates for a typical case of a single emission line plus broad-band photometry with the higher resolution ground-based spectroscopy and successfully recovered the original grism redshift estimates. In yet a different use of the ACS grism, Nilsson et al. (2011) undertook a study of Lyman-break galaxies (LBGs) at $z \sim 1$ detected in the UV by GALEX. They used grism spectra covering the 4000 Å break to measure more accurate positions of this break than could be achieved by the broad-band colors alone, which they then used to inform the SED models. The measurements yielded physical characteristics of their low-redshift sample of LBGs that were similar to LBG properties at higher redshifts.

More recently, grism spectroscopy using WFC3 on HST Early Release Science program (Windhorst et al. 2011) has yielded the discovery of 48 ELGs to a limiting magnitude of $m = 25.5$ (AB). They acquired one field observed with the G102 and G140 grisms, each at a 2-orbit depth (Straughn et al. 2011). Specific star formation rates (sSFR) were measured based on the SED fits that were low for the highest mass galaxies and that evolved with redshift, in general agreement with galaxy downsizing. (Feulner et al. 2005; Bauer et al. 2005; Elbaz et al. 2007; Rodighiero et al. 2010; Damen et al. 2009; Zheng et al. 2007).

The introduction of gravitational lensing to grism analyses is useful because it boosts the brightnesses and sizes of all objects in the background, allowing for the study of individual sources of line emission at higher signal-to-noise and higher spatial resolution. For the case of an emission line on top of stellar continuum in particular, the effect of field dilution is to smear out the continuum flux over more pixels. At the same time the compact star forming regions or galactic nuclei are also magnified but effectively remain unresolved. Thus the extended continuum is diluted with respect to the emission lines, and the detection threshold is lowered to include weaker emission line systems. Assisted by the lensing effect, the first metallicities at intermediate redshift are being measured directly (Yuan & Kewley 2009; Rigby et al. 2011). Also spatially-resolved spectroscopy is achieved, enabling measurements of star formation properties across the disk (Jones et al. 2010; Hainline et al. 2009; Frye et al.

2007).

The choice of a large, cluster-sized lens offers magnification of all galaxies in the background over fields of ~ 2 -3 arcmin in radius. Abell 1689 ($z = 0.187$, measured by Frye et al. 2007) with its large tangential critical curve of $50''$ is one of the most massive and well-studied clusters (Broadhurst et al. 2005; Limousin et al. 2007; Coe et al. 2010). The galaxies situated behind massive clusters have notoriously low surface brightnesses, and as such a space-based platform like HST is necessary for undertaking detailed and spatially-resolved studies of ELGs with fields of view larger than can be achieved with integral field unit spectroscopy from the ground. HST has already proved highly successful at identifying ELGs in a survey mode at intermediate redshifts (Xu et al. 2007; Straughn et al. 2008, 2009, 2011; Trump et al. 2011), and at high redshifts (Malhotra et al. 2005; Rhoads et al. 2009). In addition to the wide field of view, spatially-resolved spectroscopy is achieved with a resolution equal to our minimum aperture extraction width five rows or $0.25''$ and is acquired in the absence of competing strong atmospheric skylines.

Here we present a new census of ELGs in the field of the lensing cluster A1689 with the G800L grism on Advanced Camera for Surveys (ACS) on HST. This is the first space-based slitless emission line survey centered on a massive lensing cluster. One new ELG at $z \approx 0.79$ is a star forming galaxy which we designate by the paper reference Frye et al. 2012 object 1, which shortens to ‘F12.ELG1.’ This giant arc with $\sim 8''$ extent is rare for showing continuous line emitting region in several features over half its optical extent. We have taken both space- and ground-based spatially-resolved spectroscopy of this one bright ELG with a total magnitude integrated over the galaxy image of $i_{775} = 20.56 \pm 0.01$. This object is suitable for exploring the variations in physical properties across the galaxy disk.

The paper is organized as follows. In §2 we present our imaging and spectroscopic sample and data reduction techniques. In §3 we give results relating to ELGs in the cluster. In §4 we report results for new giant arc F12.ELG1. In §5 we use a lens model to construct a 1d magnification profile, compute individual magnifications for galaxies of interest, and to generate a source plane image for F12.ELG1. In §6 we discuss other field galaxies of interest, including another new sample ELG with closely spaced sources of line emission which we call ‘F12.ELG2.’ The conclusions appear in §7. We assume a cosmology with $H_0 = 70 \text{ km s}^{-1} \text{ Mpc}^{-1}$, $\Omega_{m,0} = 0.3$, $\Omega_{\Lambda,0} = 0.7$.

2. OBSERVATIONS & REDUCTIONS

2.1. ACS Grism Data

The central portion of A1689 is observed with the G800L grism with ACS on HST along with the broad band (F475W, F625W, F775W, and F850LP) exposures presented in Broadhurst et al. (2005). A single pointing is used at one position angle in a 7.1 ks exposure (3 orbits). The resulting dispersed image covers a wavelength range of 5700 - 9800 Å at a resolution of $R \sim 90$. The analysis of these images is performed using software discussed in detail by Meurer et al. (2007, hereafter M07). M07 present G800L grism observation of a well-studied

unlensed field, the Hubble Deep Field North (HDF-N), to a similar depth as our observations. They reduce and analyze this dataset in two different ways: Method A: aXe selection and reduction (Kümmel et al. 2009), which is similar to the GRAPES team pipeline, and Method B: ‘blind’ emission line source detection. Method A yields a similar set of sources as Method B, with the latter additionally yielding $>50\%$ more sources and more cases of multiple emission line sources (*i.e.* star forming regions) per object. A salient feature of Method B is its emphasis on finding emission lines in the 2d dispersed frames. This approach enables lone emission lines with weak galaxy continuum flux to be detected against the high background that is characteristic of grism images. For our aims to do spatially-resolved spectroscopy and to maximize the number of emission line sources, we perform the reductions using Method B. The primary steps of the reduction algorithm are discussed below.

The initial data reduction is performed with the Space Telescope Science Institute (STScI) ACS CCD reduction pipeline CALACS (Hack 1999), from which we use the cosmic ray rejected “CRJ” G800L images along with the individual flatfielded “FLT” broad band images (F475W, F625W, F775W, and F850LP). Since CALACS does not flatfield G800L exposures we apply our own corrections for pixel-to-pixel variations using a standard F814W flat from the STScI archive. To remove small dithers between exposures and to correct for geometric distortion we employ the ACS team pipeline Apsis (Blakeslee et al. 2003). These initial reduction steps produce geometrically-corrected and aligned grism images, which are processed further as described below. Similarly, Apsis is used to align and process the set of broadband images; the weighted sum of these is what we designate as the “direct” image.

Galaxies with strong emission lines (ELs) should be the easiest sources to identify in slitless images like our G800L data. Method B of M07 requires no prior knowledge of the location of the emitting source, although the direct image is needed to find the precise position of the emission. Moving forward from the initial reductions discussed above, we next subtract off a 13×3 median smoothed version of the dispersed image, revealing the emission line(s). We also subtract off a smoothed version of the direct image from itself. The result of this high-pass filter is to remove slowly-varying background levels, including galaxy continuum, starlight from galaxy neighbors and other sources. As detailed in M07 we have determined a geometric distortion solution relating positions in the direct image to the corresponding positions of the zeroth order in the grism image. This solution along with the measured flux scaling between direct and zeroth order images is used to mask out all significant flux from zeroth order images in the grism frame. SExtractor (Bertin & Arnouts 1996) is used to find the emission line sources in this masked and filtered grism frame. A five row segment of both of the the filtered dispersed and direct image are extracted, collapsed to 1D spectra and cross-correlated. The peak in the cross correlation gives the location of the emitting source and an estimated line wavelength. The aXe package is then used to extract a 1D spectrum from the dispersed image (prior to any filtering) using the location we found as the adopted source position. Gaussian fits to the lines

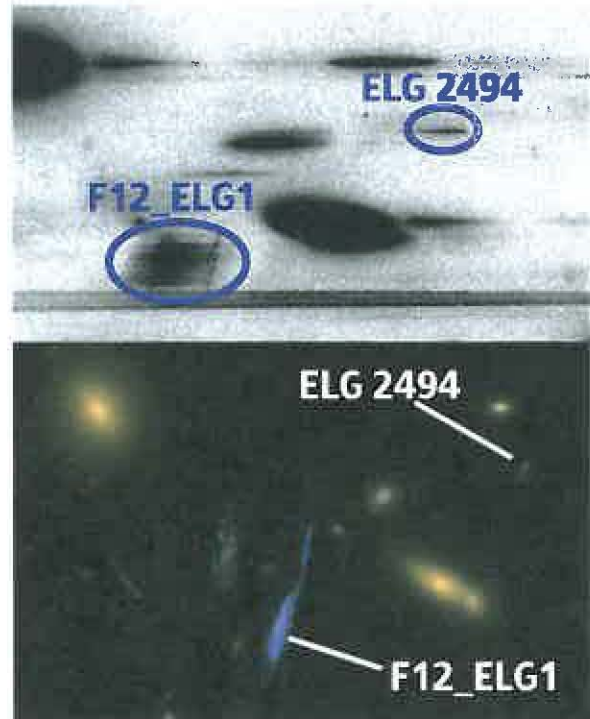


FIG. 1.— Upper panel: dispersed image of a portion of the central region of A1689, including the giant arc F12_EL G1 that is a primary result of this paper and a cluster member, ELG 2494. The dispersion direction is horizontal and the spatial direction is vertical. Note the spatially-extended emission in F12_EL G1. Three ELs are found in this single ELG and their 1d spectra are shown in Figures 5, 6, and 7. Lower panel: color image of the same portion of A1689 taken with the HST ACS *gri* filters.

in this spectrum are used to determine their final wavelength and flux values. A portion of the dispersed image that includes the spatially-resolved line emission for ELG F12_EL G1 at $z=0.79$ appears in Figure 1. We present the 1D spectrum of F12_EL G1 in §4 and §6. Figure 2 shows 1D spectra for other representative ELGs in our sample. Some line pairs can be distinguished which assist with line identifications. Notably, nebular lines [OIII] and $H\beta$ are marginally resolved in the new galaxy ELG 5158, and the close line pair $H\alpha$ and [SII] can both be identified in the new galaxy ELG 4298.

We refer to an emission feature in the dispersed image as an EL (typically $H\alpha$, $H\beta$, [OIII] or [OII]). The corresponding position in the direct image is called an emission line source (ELS). An ELS is typically an HII region or galaxy nucleus, and in some cases there is more than one EL per ELS (e.g. [OII] and [OIII]). The galaxy containing the ELS(s) is an emission line galaxy (ELG). If the galaxy is spatially resolved, there may be multiple ELSs per ELG. We identify a total of 43 galaxies (ELGs), 52 ELSs and 66 ELs. Somewhat-surprisingly, three-fourths of the ELGs are new in this well-studied cluster field. The spectroscopic results appear in Table 1. We identify nine ELGs in the cluster, 30 ELGs in the background, and five ELGs in the foreground. As the number of ELSs is larger than the number of ELGs, some ELGs have multiple H II regions spatially-resolved by the grism. In Table 2 we separate out the ELGs with two or more ELSs. The details concerning our line list

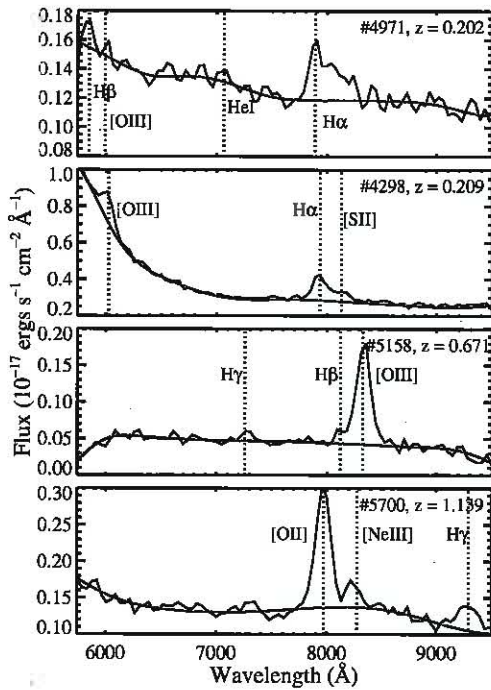


FIG. 2.— Sample spectra from our G800L ACS grism spectral catalog. The spectrum for ELG 4971 shows a detection of $H\alpha$ in a cluster member at $z=0.202$ (top panel). Despite the low spectral resolution of the grism, redshifts can still be derived even from closely spaced nebular emission features. For example, $H\alpha$ be distinguished from [SII] in some cases (ELG 4298), $H\beta$ can be distinguished from [OIII] in ELG 5158, and [NeIII] can be seen clearly with respect to [OII] in ELG 5700. Details concerning these results appear in Table 1.

and emission line properties sorted by species are given in the Appendix.

2.2. Imaging and Additional Spectroscopy

Extensive ancillary data exist to support the grism observations. Images of the central portion of A1689 were taken in several bands, as follows: *U* (DuPont Telescope, Las Campanas), *B* (NOT, La Palma), *V* (Keck II LRIS), *I* (Keck II LRIS), g_{475} , r_{625} , i_{775} and z_{850} (HST ACS), and $P_{3.6}$ and $P_{4.5}$ (Spitzer IRAC). Spectroscopy of hundreds of arclets have been acquired at several large ground-based observatories. The existing photometry and spectroscopy are discussed in detail elsewhere (Broadhurst et al. 2005; Frye et al. 2002, 2007, 2008).

Additional spectroscopy was obtained for F12.ELG1 at $z=0.79$ in 2010 May with the DEep Imaging Multi-Object Spectrograph (DEIMOS) on Keck II (Faber et al. 2003). The observations were made through a 1 arcsec slit width with the 1200 line mm^{-1} grating blazed at 10.16° and set to a central wavelength of 7800 \AA . A combination of 12 slitlets were placed together to construct the longslit mask “Long1.0B.” Two 300 s exposures were taken during dusk twilight. The seeing was $0.5\text{--}0.6''$ FWHM. Long1.0B provided a resolution of $R=5870$ measured from an isolated night sky line at 7571.75 \AA . Observations were also acquired on the Magellan Telescope I (Walter Baade) in 2009 March and 2010 March on the Inamori Magellan Areal Camera and Spectrograph

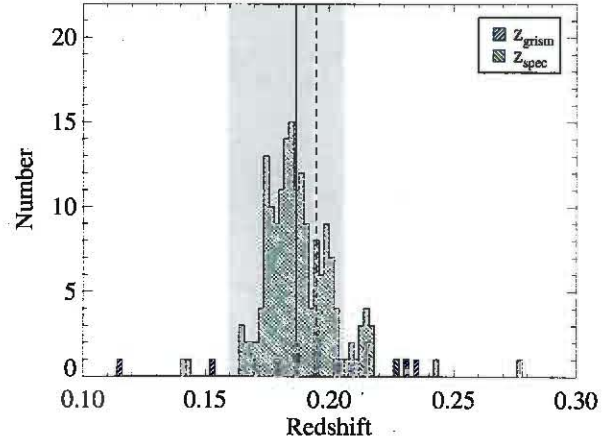


FIG. 3.— Histogram of HAEs from this sample (purple positive-slope hashed region), compared to that of all published spectroscopic redshifts in A1689 (green negative-slope hashed region). There is an extended tail towards higher redshifts which may indicate substructure and/or cluster infall. The HAEs that satisfy the redshift criteria for cluster membership are enclosed by the gray filled region. The mean redshift of all known cluster members is given by the solid line and the mean redshift of our sample cluster members is given by the dashed line.

(IMACS). One multislit mask was used with 35 targets using the $600 \text{ lines mm}^{-1}$ grism at a blaze angle of 14.67° and a central wavelength of 8410 \AA as a part of a different program (PIs Malhotra and Rhoads). The grism provided a resolution of $R = 2300$. Eight 1800 s exposures were taken in a single position.

3. THE CLUSTER

We identify 8 ELSs that are $H\alpha$ emitters (HAEs) in the redshift range $0.159 < z < 0.206$, which is the 3σ velocity dispersion redshift criteria established by Balogh et al. (2002). There are three $H\alpha$ emitting sources in the foreground of A1689, and ten $H\alpha$ emitting sources with $z > 0.206$. There is a high velocity tail in the redshift range $0.207 < z < 0.215$ that includes five ELSs that are HAEs (Fig. 3). Our sample is distinguished from the larger ground-based $H\alpha$ galaxy survey of Balogh et al. (2002) primarily by our fainter flux limit of $i_{AB} = 27.3$. Six of the galaxies that are $H\alpha$ emitters with redshifts $0.159 < z < 0.215$ are new to the literature: ELG 6621a (serendipitous discovery, see Appendix), ELG 11226, ELG 4298/4251 (ELS 4298 and ELS 4251), ELG 2494, ELG 10412, ELG 1507.

Figure 4 shows the locations of our sample cluster members (green stars) and of $H\alpha$ emitters drawn from the literature (purple diamonds). The [OII], [OIII] and Balmer line emitters from the large sample of Duc et al. (2002) appear as large open squares. The positions of other cluster members are also marked (small open squares), drawn largely from the literature as compiled in Frye et al. (2007, their Appendix). The large tilted rectangle marks the ACS field of view and the black circle shows the position of the canonical 50 arcsec Einstein ring for A1689. The HAEs presented in this paper have measured line fluxes of $-14.82 < \log f < -16.61$. The symbols are organized by total flux, with small and large symbols identifying $\log(f_{H\alpha}) \geq -16.0$. Using the relation in Kennicutt (1998) we compute star formation rates

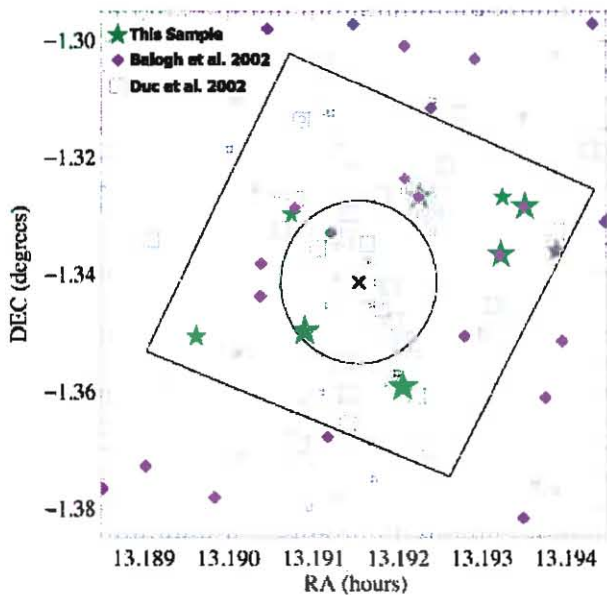


FIG. 4.— Map of HAEs in A1689 from our census (green stars) and from the sample of Balogh et al. (2002) (purple diamonds). Our HAEs are further organized by flux, with small and large symbols representing objects with $\log(f_{H\alpha}) < -16.0$ and $\log(f_{H\alpha}) \geq -16.0$ respectively. The HAEs are well-distributed azimuthally, and appear to be underpopulated at smaller cluster-centric radii. The positions of cluster members with absorption redshifts from Duc et al. (2002), and the few that could be found in the literature, are indicated by the open-squares and concentric-squares, respectively. The canonical Einstein ring is indicated by the large black circle, with cluster center at ‘X.’

of $0.017 < \text{SFR} < 1.1 M_{\odot} \text{ yr}^{-1}$.

The positions of the ELGs cover the far-field reasonably well. Of the 30 $H\alpha$ emitters comprising this sample plus those drawn from the literature, only one is located close in to the cluster center. This is a new ELG presented in this paper, ELG 4298/4251, which with $i_{775} = 21.74 \pm 0.01$ is not reported in the large $H\alpha$ survey of Balogh et al. (2002) as it is fainter than their I -band magnitude-limit of 19.3. The preferential placement of $H\alpha$ emitters in the cluster outskirts appears to satisfy the general trend of increasing star fraction as density decreases, and is biased as a result of confusion from a high source density in the cluster interior and small number statistics. It is interesting to note that there is an excess of galaxies detected at $100 \mu\text{m}$ with Herschel that is distributed as a swath running NE-SW across their field (Haines et al. 2010). Evidence of filamentary structure is not seen in our galaxy census which is less than one-tenth the field size of their sample.

4. F12.ELG1: THE GIANT ARC AT $Z=0.7895$

4.1. Galaxy Properties Measured from the HST Grism

The image and spatially-resolved G800L spectra of F12.ELG1 with a visual extent of > 8 arcsec and a magnification provided by the cluster of a factor of 4.5 appear in Figure 5. This is one of a handful of the brightest star forming galaxies at $z \sim 1$ ($M_B = -21.3$), allowing for a study of one ELG in detail at intermediate redshift. The HST grism spectroscopy shows three separate emission line sources (ELSs) as ELS 20002 (‘A’), ELS 10638 (‘B’), and ELS 10640 (‘C’). Each ELS has at least two emission

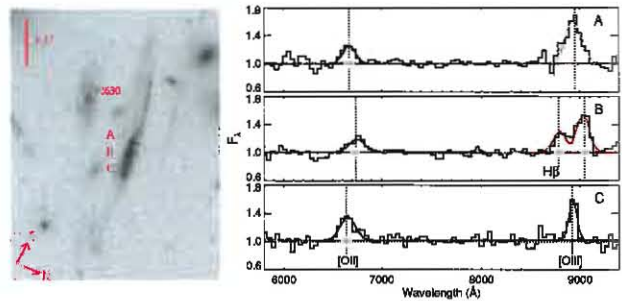


FIG. 5.— i_{775} image and flux-normalized G800L spectra are shown for the bright giant arc F12.ELG1 at $z=0.790$. The spatially-resolved spectroscopy corresponds to the three sources of line emission along the long axis of this galaxy, ELS 20002 (‘A’), ELS 10638 (‘B’), and ELS 10640 (‘C’). Components B and C are $0.27''$ apart, corresponding to an intrinsic separation of only 0.5 kpc. The flux of [OIII] relative to $H\beta$ is highest in the center, and from follow-up spectroscopy we find a region near the center to be best-fit by an AGN (See §6.1 and Fig. 9). The shift in the line peaks between components A, B, and C is a result of large uncertainties in the zero-point of the wavelength solution. We detect emission in a second galaxy near in projection to F12.ELG1, labeled as ELS 2630 at $z = 0.335$.

lines: [OII] $\lambda\lambda 3726, 3729$ and [OIII] $\lambda\lambda 4959, 5007$, with the central knot ‘B’ also showing $H\beta$ line emission. The line fluxes and rest equivalent widths are given in Table 1. A fit to the line centroids of the emission features in Component A yields a redshift of $z=0.790$, confirming the redshift in Duc et al. (2002). Knots A and B have a separation at the source of 1.5 kpc, while knots B and C are separated by only 0.5 kpc. There appear to be significant redshift differences between knots A, B, and C. These are likely to be owing to misidentification of the precise x position of the ELSs, which will translate into a wavelength error.

4.2. Galaxy Properties Measured from Ground-based Spectroscopy

In our Keck and Magellan spectra of F12.ELG1 we see line emission from star forming regions across a continuous $4''$. From the 1D spectroscopy of this extended line emission we recover all the emission features of the HST grism spectrum, and detect as well additional emission lines. We identify: [O II] $\lambda 3726$, [O II] $\lambda 3729$, [O III] $\lambda 4959$, [O III] $\lambda 5007$, $H\beta$ and $H\gamma$, with $H\delta$, $H\epsilon$, $H\delta$, and [Ne III] $\lambda 3869$, and weak [C III]/[C IV] $\lambda 4650$ (in the Magellan spectrum). While the results are similar for our two ground-based datasets, we will focus primarily on the Keck spectrum herein with its higher spectral resolution and flux calibration taken with a standard star at the time of the observations. The line fluxes for the strong emission lines for the Keck spectroscopy appear in Table 3.

A Gaussian fit to [OII] and [OIII] in our Keck spectrum yields a new systemic redshift of $z=0.7895$. The line width is estimated from the fit to the [OIII] $\lambda 5007$ line, and is found to be $\Delta v = 500 \text{ km s}^{-1}$ after subtraction of the instrumental resolution. This is the line width set for all other emission features. To account for the slightly asymmetric line profile of the [OIII] $\lambda 5007$ line owing to an adjacent sky line, the flux value is taken from the Gaussian fit rather than from the data values. The [OIII] $\lambda 4959$ line also suffers from its unfortunate

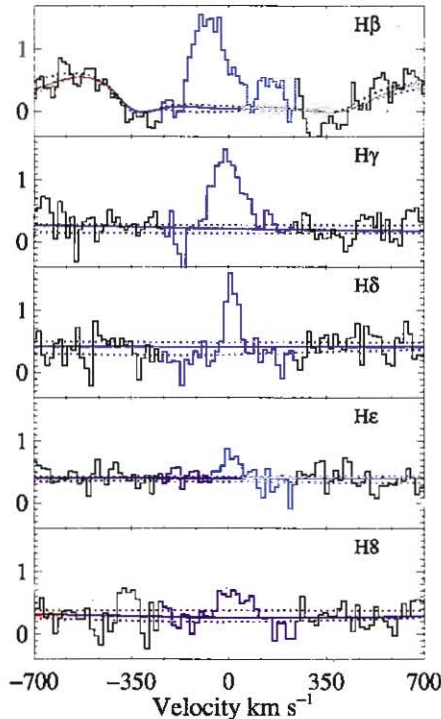


FIG. 6.— Stackplot of the Balmer family of emission lines for F12.ELG1, as labelled. Most notable is the rare detection of Balmer transmission lines continuously in emission from H β through H8, indicating a young starburst event. The continuum fit plus uncertainties are given by the red solid plus red dashed lines. The velocity range of the line (in blue) corresponds to $-250 \text{ km s}^{-1} < v < +250 \text{ km s}^{-1}$ with reference to the systemic redshift of $z = 0.7895$. These data are from our Magellan follow-up spectroscopy and the units are in normalized counts. All spectra have been corrected for extinction by dust.

placement relative to a skyline. In this case the well defined ratio of [OIII] $\lambda 5007$ to [OIII] $\lambda 4959$ of 3:1 is used for any calculations involving the sum of the fluxes or equivalent widths of these two lines. For all other line features, the values are measured directly from the data. The Balmer transition lines H β through H8 are shown in Figure 6. The velocity range over our 500 km s^{-1} measurement width is shown in blue and varies from $-250 \text{ km s}^{-1} < v < +250 \text{ km s}^{-1}$ with reference to the systemic redshift of $z = 0.7895$. This large family of Balmer features all in emission is rare for an extragalactic source and signals the early stages of a major starburst.

Our Keck spectrum has at best only a slight continuum break at rest-frame 4000 \AA . Balogh et al. (1999) define this break $D_n(4000)$ as the ratio of the average flux density in the wavelength band $4000\text{--}4100 \text{ \AA}$ to the $3850\text{--}3950 \text{ \AA}$ band. We measure a break index of $D_n(4000) = 0.96 - 1.0$ after first masking out the strong [Ne III] $\lambda 3869$ and H8 emission lines. This near lack of a continuum depression indicates a dominant population of hot young stars. The population synthesis models of Bruzual & Charlot (2003, hereafter BC03) provide a value of $D_n(4000)$ for each spectral energy distribution (SED; see §4.3 for a description of our model). For a reasonable subset of models over four metallicities ($0.2Z_\odot$, $0.4Z_\odot$, Z_\odot , and $2.5Z_\odot$) and a range of star formation histories, we have set an initial constraint on the age of

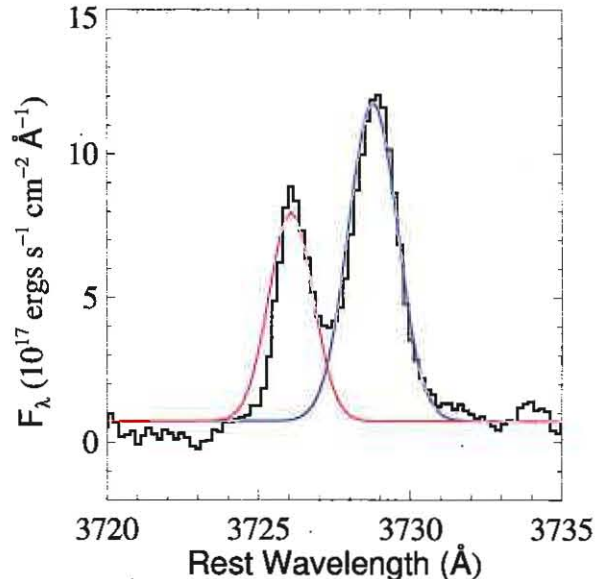


FIG. 7.— Rest-frame resolved [OII] $\lambda\lambda 3726, 3729$ emission lines from F12.ELG1, with Gaussian fits to the features overlaid. The ratio of the relative strengths of the two lines allow the calculation of the electron density $N_e = 980 - 1280 \text{ cm}^{-3}$. These data are from our Keck DEIMOS follow-up spectroscopy.

the dominant stellar population of the galaxy to a range of $6 \text{ Myrs} \leq t \leq 100 \text{ Myrs}$. Note that any contribution from AGN continuum light would operate to raise the value for $D_n(4000)$, and hence lead to an underestimate in the age of the galaxy (Kauffmann et al. 2003). We infer from spatially-resolved analysis that this object is most likely dominated by star formation but also shows evidence of a harder ionizing source (see §6).

The [OII] $\lambda\lambda 3726, 3729$ doublet is spectrally-resolved in our Keck DEIMOS data, and this is useful as these are density sensitive lines (Fig. 7). The intensity ratio is measured to be 1.44, which for a typical temperature of $T = 10,000\text{--}20,000 \text{ K}$ equates to $N_e = 980 - 1280 \text{ cm}^{-3}$. This is a factor of ~ 3 higher than the star forming galaxies in the Kobulnicky & Kewley (2004) sample with $0.3 < z < 1.0$, and is consistent with ELG samples at $z \sim 2$ (Lehnert et al. 2009; Hainline et al. 2009). These, and all other fluxes in this paper are corrected for underlying stellar absorption, extinction by dust, and cluster magnification as described in §4.3 and §5.

4.3. The SED, Underlying Stellar Absorption, and Reddening

The hydrogen Balmer features consist of both a nebular emission and a stellar absorption term. The emission lines tend to weaken towards higher level transitions owing to the sum of a rapidly decreasing nebular emission line strength with decreasing wavelength and an equivalent width of the stellar absorption component that at best increases only modestly with wavelength. To make a correction for the underlying stellar absorption we compute an intrinsic SED model template and then subtract it from the galaxy spectrum in a manner similar to that of Tremonti et al. (2004). We note that as our object is rare for showing H β through H8 all in emission, the underlying stellar absorption is not expected to be a major contaminant.

Our optical through infrared photometry is used to construct the matching SED model. We delens the photometry using a magnification factor of 4.5. The observed (unlensed) photometry of F12.ELG1 is as follows: $U=21.05\pm 0.16$, $B=21.22\pm 0.17$, $V=21.08\pm 0.15$, $g'=21.06\pm 0.08$, $r'=20.87\pm 0.01$, $i'=20.56\pm 0.01$, $z'=20.44\pm 0.01$, $P_{3.6}=20.11\pm 0.07$ and $P_{4.5}=20.46\pm 0.08$. Our measurements of the Balmer decrement allow a bracketed range of model stellar ages $6 < t < 100$ Myr (see §4.2). This constraint is in keeping with our detection of higher level Balmer emission lines, as population synthesis models for star-forming galaxies predict for these features an increase with evolution up to 500 Myr (González Delgado et al. 1999). Our model fitting approach allows for a range of metallicities and assumes a single starburst model with a range of decay rates τ and a star formation rate that depends exponentially on τ as follows: $SFR(t) \propto \exp(t/\tau)$. A summary of our parameter ranges are as follows:

- $\tau = 0.1, 0.2, 0.3, 0.5, 1$ and 5 Gyr
- $t = 6 - 100$ Myr
- $Z = 0.2Z_{\odot}, 0.4Z_{\odot}, 1Z_{\odot}, 2.5Z_{\odot}$

For each fixed τ , t , and Z , two parameters are fit to the data: color excess $E(B - V)$, and stellar mass M_* . A suite of models are constructed over the allowable parameter space, and each model is corrected for dust extinction. We compute synthetic photometry for comparison with the observed photometry until the lowest value of reduced χ^2 is obtained, as is described in detail in Frye et al. (2008). Our best fit model estimate yields $E(B - V) = 0.45$ and $M_* = 2 \times 10^9 M_{\odot}$ for a young stellar age of $t = 8$ Myrs, $Z = 0.4Z_{\odot}$ and $\tau = 5$ Gyr. After redshifting and binning to the correct spectral resolution, we measure a correction in rest-frame equivalent width of $W = 1.5\text{\AA}$ for the $H\beta$ line. All Balmer emission lines include this correction for underlying stellar absorption. Our measured emission line rest equivalent widths are too low to affect the SED fits, in contrast to the large equivalent widths found in Atek et al. (2011). Note although t is less than the estimated galaxy crossing time by a factor of ~ 2 , we find the BC03 models to provide an adequate fit to the data for our purposes of determining estimates for stellar absorption.

The attenuation of the intrinsic light due to dust is calculated from a standard curve, which for a starbursting galaxy is given in Calzetti et al. (2000), their Eq. 4. Dust extinction is calculated using the Balmer decrement method, whereby a pair of emission lines with a well-defined intrinsic ratio from atomic theory such as Balmer lines is compared with the data. We use $H\beta$ and $H\gamma$ from our Keck dataset, and attribute any deviation from the intrinsic value to dust. After correcting for the underlying stellar absorption, we measure $f(H\gamma)/f(H\beta) = 0.321$. For an intrinsic ratio of $f(H\gamma)/f(H\beta) = 0.469$ given by Osterbrock (1989), we compute $E(B - V)_{gas} \approx 0.78$. This value is different from the color excess measured by SED fitting of $E(B - V) = 0.45$. Some of this discrepancy is owing to incomplete areal coverage of the galaxy image. We adopt the more general value measured from the SED modeling for this study.

4.4. Spectral Classification

The spectral classification of ELGs at low redshift can be determined from emission line diagnostic diagrams such as the classical Baldwin, Phillips & Terlevich (BPT) diagram (Baldwin et al. 1981). The BPT diagram is based in part on $H\alpha$ and $[N II]$ lines which are redshifted out of the optical passband for $z \geq 0.4$. Classification systems based on bluer emission lines are also well developed (Lamareille et al. 2004, 2009; Pérez-Montero et al. 2009; Lamareille 2010; Rola et al. 1997; Marocco et al. 2011). Marocco et al. (2011) revise the blue emission line scheme of Lamareille (2010). Their samples are derived from the Sloan Digital Sky Survey (SDSS) and do not include a correction for dust extinction.

We classify F12.ELG1 for our ACS grism (G800L) dataset for which we have complete coverage of the emitting line region. We correct all fluxes for underlying stellar absorption and dust extinction and sum up the flux over all three ELSs. Under the Marocco et al. (2011) scheme, which involves the line ratios $f([OIII])/f(H\beta)$ and $f([OII])/f(H\beta)$, F12.ELG1 is situated in the intermediate region that includes both star-forming galaxies (SFGs) and Seyfert 2 objects. In a different classification scheme, Pérez-Montero et al. (2009) use also the VVDS samples but instead consider the ratios of $f([OII])/f(H\beta)$ and $f([Ne III])/f(H\beta)$ after accounting for dust extinction. With this diagnostic set, F12.ELG1 is placed in a region that includes SFGs and the uncertainty domain between SFGs and AGNs.

The detection of additional spectral features similarly suggests that F12.ELG1 is in a position intermediate between star forming and AGN source types. We detect $[CIII]/[CIV]\lambda 4650$ commonly seen in AGN and measure a flux ratio of $[NeIII]/H\beta \approx 0.6$, a value consistent with excitation by a hard ionizing source (Osterbrock 1989). At the same time we fail to detect $[NeV]\lambda 3426$ and $[HeII]\lambda 4686$, two emission lines typically associated with AGN, although the signal-to-noise is poor at the expected position of $[NeV]\lambda 3426$ owing to its placement on top of a strong skyline. Note the AGN diagnostic line $[NeV]\lambda 3346$ is blueward of our passband. As for the common nebular lines, the flux ratio $f([OIII])/f(H\beta)$ is low in the center, a trend that runs contrary to the expected behavior of a central AGN (Fig. 5). Interestingly, the Balmer decrement is at best only marginally detected, which when used as an additional diagnostic places this object as an SFG for any value of $[OII]$ and $[NeIII]$ (Marocco et al. 2011). We conclude that there is at least a strong star forming component to F12.ELG1, and that the AGN interpretation cannot be ruled out. We will use spatially-resolved spectroscopy to address the possibility that this object supports AGN-like activity in §4.7.

4.5. Gas-phase Oxygen Abundance

The gas phase oxygen abundance is estimated from the metallicity sensitive rest-frame optical emission lines. The direct measurement from the $[OIII]\lambda 4363$ line typically seen in metal-poor galaxies is not detected in any of our spectroscopy. The indirect measurement using emission line ratios involving $H\alpha$ is redshifted out of our passband. From the available emission lines we can compute $R_{23} = (f([OII]\lambda 3727) + f([OIII]\lambda\lambda 4959, 5007))/f(H\beta)$ and

$O_{32} = (f([\text{OIII}]\lambda 4959) + f([\text{OIII}]\lambda 5007)) / f([\text{OII}])$. $R_{23} = 4.6^{+2.3}_{-1.5}$, and $O_{32} = 0.96^{+0.39}_{-0.28}$ for the G800L dataset and after first correcting all line fluxes for underlying stellar absorption, reddening and cluster magnification. The uncertainties reflect 1σ errors in the noise and continuum placement.

The calculation of gas-phase oxygen abundances from R_{23} is complicated by its double-valued behavior, with a given value representing either the metal-poor lower branch, the metal-rich upper branch, or a transition at $12 + \log(\text{O}/\text{H}) \approx 8.4$. We measure values for several empirical calibrations. Our value for R_{23} yields an abundance of $12 + \log(\text{O}/\text{H}) = 8.1$ (lower branch) and 8.9 (upper branch) Kobulnicky & Kewley (2004). For Tremonti et al. (2004) as adapted from the method of Charlot & Longhetti (2001) we obtain $12 + \log(\text{O}/\text{H}) = 8.8$ (upper branch). For Zaritsky et al. (1994) we measure $12 + \log(\text{O}/\text{H}) = 8.8$ (upper branch). Finally, we compute $12 + \log(\text{O}/\text{H}) = 7.8$ (lower branch) and 8.7 (upper branch) for McGaugh (1991) as given by Kobulnicky & Johnson (1999). F12_ELG1 is consistent with being on either branch.

Of the available emission features, the secondary indicator $[\text{NeIII}]$ can break the metallicity degeneracy (Nagao et al. 2006). We compute $f([\text{NeIII}]) / f([\text{OII}]) = 0.05^{+0.01}_{-0.07}$, which has a best-fit polynomial correspondence value of $12 + \log(\text{O}/\text{H}) = 8.8 \pm 0.2$. Our value is close to the solar value of $12 + \log(\text{O}/\text{H}) = 8.66$ (Allende Prieto et al. 2002; Asplund et al. 2004). It also overlaps with the range of values obtained from current metallicity history studies at $z=1-2$ of $12 + \log(\text{O}/\text{H}) = 8.3 - 9.0$ (Lamareille et al. 2006; Liu et al. 2008; Hainline et al. 2009). In turn, all values are higher than those of direct measurements from strongly-lensed high- z galaxies (Yuan & Kewley 2009; Rigby et al. 2011).

4.6. Star Formation Rate

We estimate the star formation rate in two ways: (1) by extrapolating the intrinsic $\text{H}\beta$ line flux into an estimate of the $\text{H}\alpha$ flux, and (2) from the intrinsic (corrected for reddening and lensing magnification) $[\text{OII}]$ line flux. Although our observations do not cover the most reliable tracer of star formation, $\text{H}\alpha$, one can infer the $\text{H}\alpha$ line flux from the $E(B-V)$ value and the intrinsic flux ratio between $\text{H}\beta$ and $\text{H}\alpha$ (Osterbrock 1989). We estimate the intrinsic fluxes for $\text{H}\alpha$ to be: $f(\text{H}\alpha) = 1.4^{+0.53}_{-0.61} \times 10^{-15}$ ergs $\text{s}^{-1} \text{cm}^{-2}$ and $f(\text{H}\alpha) = 2.1^{+0.38}_{-0.33} \times 10^{-16}$ ergs $\text{s}^{-1} \text{cm}^{-2}$ for the Keck and HST G800L observations, respectively. The SFR can be measured using the relation starting from Kennicutt (1998): $\text{SFR}(M_{\odot}/\text{yr}) = 7.9 \times 10^{-42} f(\text{H}\alpha) * 4\pi D_L^2$ ergs s^{-1} . For the Keck observations we measure $\text{SFR} = 31^{+11}_{-13} M_{\odot} \text{yr}^{-1}$. For the HST G800L observations there is insufficient spectral resolution to detect $\text{H}\beta$ in every ELS, making our value of $\text{SFR} \gtrsim 6.5 M_{\odot} \text{yr}^{-1}$ a lower limit. We will adopt the value for the SFR from the Keck observations for this study.

Calibration of the star formation rate using the intrinsic $[\text{OII}]\lambda 3727$ line is more challenging, as it is more sensitive to reddening, metallicity and ionization parameter. Kewley et al. (2004) present an algorithm that takes these dependencies into account, especially for high gas-phase oxygen abundances which apply to our case

($\log(\text{O}/\text{H}) + 12 > 8.4$). Their Equation 14 for SFR is based on ionization parameter and gas-phase oxygen abundance. Using this equation yields $\text{SFR}_{[\text{OII}]} \approx 3 M_{\odot} \text{yr}^{-1}$ for the G800L grism dataset, a value that is small compared to estimates based on $\text{H}\beta$ flux. We will adopt the value for the SFR from the $\text{H}\beta$ flux for this study as its relation to $\text{H}\alpha$ is better understood, and plan to measure SFR directly by $\text{H}\alpha$ in grism observations with VLT SINFONI in an upcoming paper. Finally, we compute $\text{sSFR} \approx 20 \text{Gyr}^{-1}$.

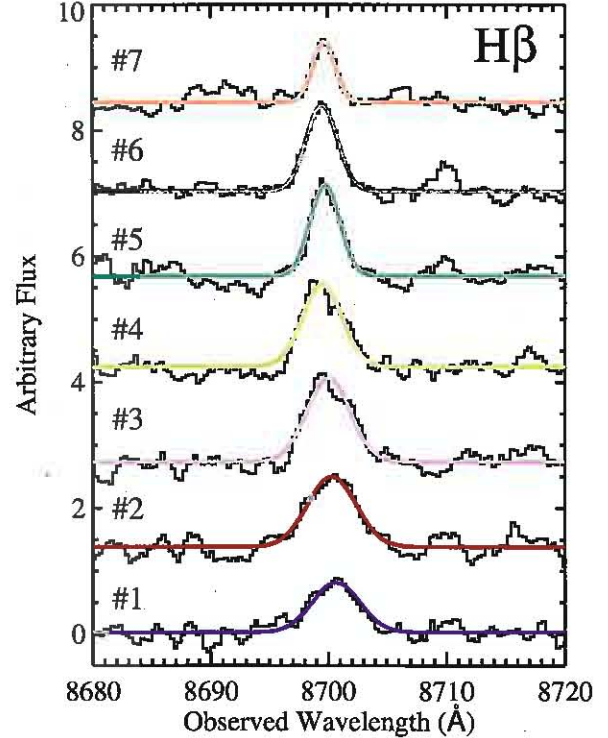


FIG. 8.— Spectra centered on the $\text{H}\beta$ emission line are plotted for each of the seven slices in our spatially-resolved Keck spectrum of F12_ELG1 at $z = 0.7895$. The colors are matched to the colors in Fig. 9. The line fits are used to determine the central wavelengths and FWHM's. We find a small Doppler shift in the line centroid across the bins.

4.7. Spatial Trends in F12_ELG1

The image of this giant arc is noticeably bisected into a broad, line-emitting clump and a long extended tail. Line emission is detected only in the clump. We have spatially-resolved spectroscopy with sufficient angular resolution to subdivide the line emitting clump into seven contiguous bins of $0.6''$ each, or equivalently 1kpc each after correcting for a magnification factor of 4.5. Each bin is assigned a different color. The bins have the following assignments: Bin 1 (purple), Bin 2 (rose), Bin 3 (lavender), Bin 4 (light green), Bin 5 (dark green), Bin 6 (olive), and Bin 7 (orange). We extract the seven spectra and compute line fluxes, line centroids and velocity widths for common emission lines. A sample stack plot centered on the position of $\text{H}\beta$ in particular is shown in Figure 8, and an image of F12_ELG1 with the seven bins overlaid appears in the top panel of Figure 9.

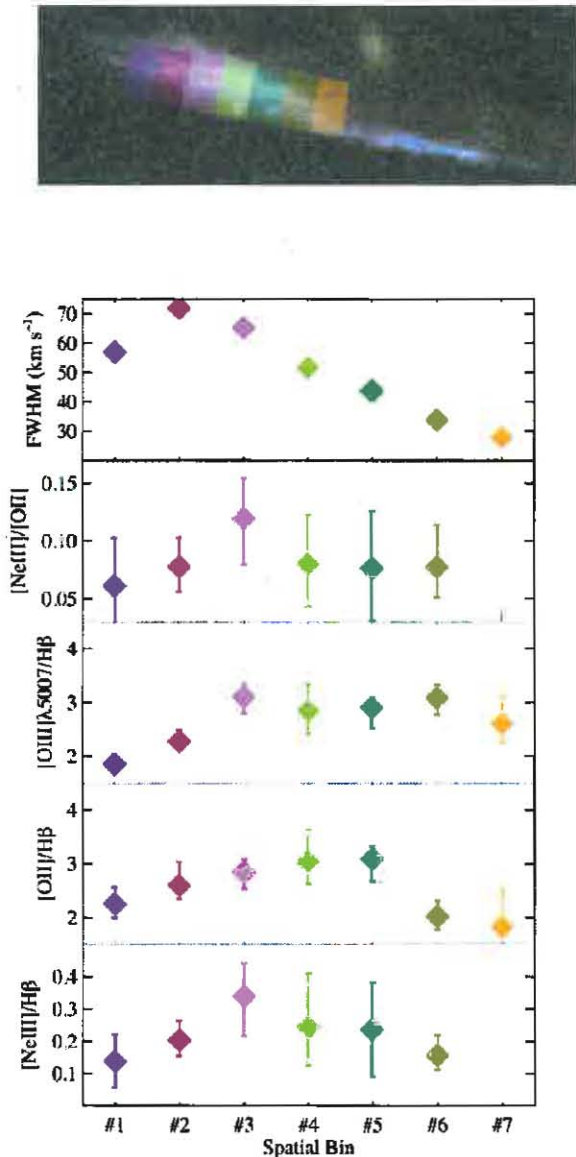


FIG. 9.— *gri* image of F12_ELG1 at $z = 0.7895$, with trends in the FWHM of a strong emission line and metallicity dependent line ratios shown along the substructure of this giant arc. Each spatial bin covers $0.6''$ or ~ 1 kpc (intrinsic). The FWHM peaks at Bin 2, which is taken to be the dynamical center. The metal fraction peaks in Bin 3, which is offset from the dynamical center. The metal line ratios in Bin 3 admit the possibility of an AGN. This asymmetrical AGN-like behavior may be a result of shocks in the direction of the long extended tail.

The velocity dispersion σ is derived from the FWHM of the $H\beta$ line and based on the assumption that the line width is set by the spread of velocities of the line emitting gas about the local central mass. The instrumental profile is subtracted off of the FWHM in quadrature, and then σ is computed as follows: $\text{FWHM}/2.355 \cdot c/\lambda_{\text{obs}}$. There should be a peak at the galaxy’s center of mass if the object is supported by a central mass pulling on the stars. For F12_ELG1 the peak is at Bin 2, making this location the likely location for the galaxy nucleus (Fig. 9). The uncertainties in σ come from continuum fitting and are less than the size of the plotting symbols. It is inter-

esting that the $H\beta$ line centroid *blueshifts* relative to the mean value along the galaxy, from $\Delta v = +35 \pm 5 \text{ km s}^{-1}$ for bin 1 to $\Delta v = -13 \pm 5 \text{ km s}^{-1}$ in bin 7. These results are similar to what is also seen across the lensed galaxy Lens22.3 at $z = 1.7$ (Yuan & Kewley 2009). From the velocity dispersion one can compute a rough value for the dynamical mass of $\sim 2 \times 10^9 M_{\odot}$. This value is consistent with our estimated stellar galaxy mass from SED-fitting. We measure $M_B = -22.2$, and in turn obtain an estimate of the mass to light ratio of $M/L \approx 1$. Our low measured M/L and stellar mass is consistent also with our stellar age by SED fitting of $t = 8 \text{ Myr}$. This is similar to the work of van der Wel et al. (2005) who find a low M/L and low stellar mass at $z \sim 1$ to be correlated with a young stellar age.

The trends of various metallicity-dependent line ratios across the galaxy are also shown in Figure 9. We retain the same bin coloring scheme and apply the same modest correction for stellar absorption and extinction to each bin as computed in §4.3. While the peak in the FWHM is at Bin 2, there is a temptation to find a peak over the metal line ratios at Bin 3, and a drop off to the left-hand-side (Bins 1 and 2). We derive below a number of interesting results by a comparison of values in Bin 3 with the mean of Bins 1 and 2 (Bins 1-2). By Marocco et al. (2011) Bin 3 encompasses the composite star forming galaxy (SFG)/Seyfert 2 and Seyfert 2-only regions of their $f([\text{OIII}]/H\beta)$ vs. $f([\text{OII}]/H\beta)$ H II excitation diagram. Meanwhile Bins 1-2 yield a different result, and reside entirely in the SFG/Seyfert 2 region. By the approach of Pérez-Montero et al. (2009), which includes $[\text{NeIII}]$, Bin 3 plus uncertainty region lies in the transition region between SFGs and AGNs while Bins 1-2 plus uncertainty region lies entirely *inside* the SFG region. We conclude that the disk-like Bins 1-2 are consistent with an SFG while Bin 3 exhibits AGN-like behavior. These strong metal line ratios that are driven by a hard ionizing source and are offset by $\sim 1 \text{ kpc}$ from the peak of the velocity dispersion appear to be best explained by shocks in the direction of the galaxy tail (Bins 4-7).

The values for $[\text{OIII}]/H\beta$ are large all across the galaxy, and are also higher in Bin 3 compared to Bins 1-2. In Bin 3 we measure $\log(f([\text{OIII}])/f(H\beta)) = 0.49 \pm 0.04$. There is only a hint of a trend in the behavior of $[\text{NeIII}]/H\beta$, but it is worth noting that $[\text{NeIII}]/H\beta$ is high in the central three bins, and for Bin 3 in particular the value is consistent with 0.4, a value commonly associated with AGN (Osterbrock 1989). It is tempting to say the disk-like Bins 4-7 also show a decline from Bin 3, and if so then the various line ratios are not falling off as rapidly as in Bins 1-2. We speculate that there is a moderately elevated metal fraction in Bins 4-7 that may be a result of increased star formation activity in the direction of the galaxy tail, indicating possible harassment in the galaxy’s star formation history.

If Bins 4-7 indeed lead towards a galaxy tail, then one can ask the question of which are the likely culprits for past interactions? F12_ELG1 has neighbors roughly centered in redshift at the systemic redshift of $z=0.7895$. There are seven galaxies with spectroscopic redshifts of $0.7625 < z < 0.8175$ distributed over a field in the image plane of ≈ 3.5 arcmin on a side, which for a mean magnification of $\sim 4\times$ yields a physical size in the source plane of 0.8 Mpc . This structure or filament may con-

tribute to the compound lensing effect at the $1''$ level that is important for doing precision cosmology with clusters (Jullo et al. 2010).

4.8. Evolution of F12_ELG1

In sum, with its high sSFR corresponding roughly to a cold gas fraction of ~ 0.7 (Reddy et al. 2005), its low mass, and presence of many Balmer series emission lines, this strongly-lensed but otherwise ordinary galaxy would appear to be caught at the beginning of a major burst of star formation. This is consistent with the picture of van der Wel et al. (2011) in which $\sim 1/2$ the stars in a typical field galaxy are formed in only $\sim 2-3$ bursts that produce the stellar population in a $M_* = 10^9 M_\odot$ by $z \sim 1$. F12_ELG1 also looks similar to the objects in Kriek et al. (2009) that are AGN hosts of size ~ 1 kpc.

F12_ELG1 has similar ionization properties compared to other $z=1-2$ star-forming galaxies, and as a group such objects have elevated ionizations compared to the local galaxy population. It is thought that galaxy feedback must play a role in understanding these differences. One possible explanation is that many intermediate redshift galaxies may harbor weak AGNs (Wright et al. 2010; Trump et al. 2011). F12_ELG1 has elevated metal-line ratios consistent with an AGN that are interestingly offset from the dynamical center of the galaxy. Given this extended tail in the same direction, we interpret the asymmetrically-situated AGN-like region of this galaxy as shock excitation possibly as a result of a past galaxy interaction. The line ratios decrease towards the outer disk on both sides of the peak in this one galaxy, similar to the spatially-resolved spectroscopy of another giant arc at intermediate redshift, the ‘Clone’ (Jones et al. 2010). By contrast, in a sample of 50 intermediate redshift ELGs with integral field unit spectroscopy a significant fraction showed the opposite trend (Queyrel et al. 2011).

5. CLUSTER LENSING

Abell 1689 is one of the best studied clusters in the literature, with several published lens models (Broadhurst et al. 2005; Limousin et al. 2007; Halkola et al. 2006; Leonard et al. 2007; Zekser et al. 2006; Coe et al. 2010). In this work we adopt the model presented in Broadhurst et al. (2005), which is constructed from 30 multiply-imaged galaxies with supporting multiband photometry of the field and spectroscopy of a representative sample of the arcs. The Broadhurst et al. (2005) model compares favorably with measurements using an independent model from the literature (Limousin et al. 2007).

We use our lens model for A1689 to construct an azimuthally-averaged magnification profile to predict source magnifications (μ) owing to strong lensing. We measure the magnification straightforwardly by tabulating a grid from the best-fitting magnification map that spans roughly the ACS field of view ($190''$ on a side). Our resulting magnification profile is shown in Figure 10, corresponding to the measured mean redshift of background objects in the field drawn from the literature (Frye et al. 2007) and references therein.

The median magnification (μ) peaks at $\mu=35$ and has a long tail extending towards large radial distances. We report the median magnifications rather than the mean

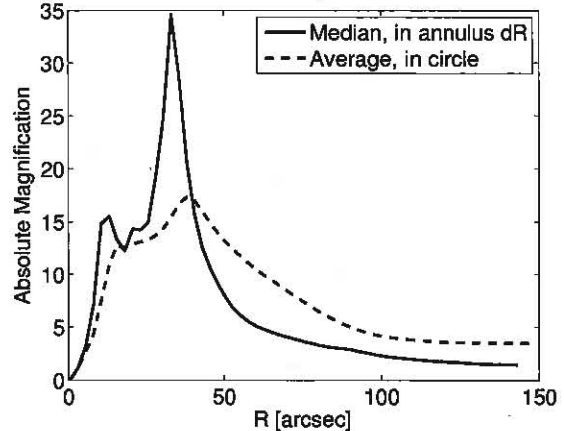


FIG. 10.— Radial magnification profiles for the average magnification inside a circle of radius R (dashed line), and the median magnification in an annulus of $2.5''$ about R (continuous line) assuming in each case a mean source redshift of $z = 0.8$ as drawn from the literature (Frye et al. 2007). The primary and secondary peaks appear at the locations of the tangential and radial critical curves, respectively. The net advantage of this lensed field is a factor of ~ 4 integrated over a large $R = 150''$ (0.5 Mpc) radius.



FIG. 11.— Left-hand side: two-dimensional magnification map of the lens A1689 (contours) overlaid on the gri image of the blue giant arc at $z = 0.7895$. The linear magnification varies differentially from $\mu = 4 - 5$ along the arc, enhanced locally by the nearby cluster elliptical at right. Seven non-overlapping bins of substructure are overlaid as colored rectangles in both the image and source planes. The bins are oriented and have a size corresponding to the position angle and slit-width of the observations. Right-hand side: the reconstructed source plane image yields a single nucleus with an extension that may be a tidal tail.

magnifications so as not to include the high model magnifications exceeding $\mu=100$. The magnification of both curves is high outside the tangential critical curve of $50''$, even out to large radii of $R=150''$ (≈ 0.5 Mpc), where the median absolute magnification is $\mu \approx 4$. Given this magnification profile, all the sources in our catalog and behind the cluster are likely magnified. The magnification is computed in detail for two giant arcs of interest below.

The magnification contours for F12_ELG1 are laid down onto the HST gri image in Figure 11. The contours increase in the direction of the two massive cluster ellipticals appearing just above the “ $\times 10$ ” magnification label and in the upper left-hand corner of the image. We compute a magnification that increases from a factor of four to five along the long axis of the arc, with a mean value that we use for this paper of $\mu = 4.5$. This value supercedes a previous measurement (Frye et al. 2002), as this one is derived explicitly from the lens model. No

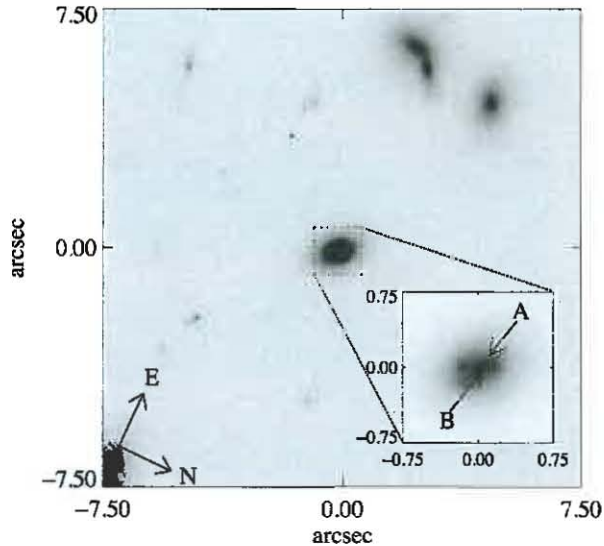


FIG. 12.— Image in i_{775} of F12.ELG2 (center). The inset image is a close-up of the region indicated by the dotted lines that contains two emission line sources (ELS 20004 ‘A’ and ELS 11085 ‘B’). ELSs A and B have a close angular separation of $\theta \approx 0.2''$, and other knots are also detected in the vicinity of this elliptical galaxy. We show the grism spectroscopy in Figure 13.

counterarcs are predicted for this arc which is not situated close the expected positions of the critical curves. The reconstructed source plane image shows one bright compact region of size $\sim 1''$ and an extended tail.

6. OTHER FIELD GALAXIES

6.1. Double-peaked $H\alpha$ in F12.ELG2

We report new ELSs detected with the ACS G800L grism which have close angular separations. They are: ELS 20004 ‘A,’ ELS 11085 ‘B’ (Fig. 12). We designate this group of sources as ‘F12.ELG2.’ Sources A and B have an angular separation of $\approx 0.21''$, and are resolved despite the angular separation being slightly smaller than our predicted spatial resolution of $R_0 = 0.25''$ set by our algorithm that extracts a minimum of five spatial pixels centered on an emission line. The spectrum for component A shows two emission line peaks with similar flux amplitudes. The spectrum for component B shows a single emission line with an extended red tail that appears to be associated with at least some of the same emission sources as in component A (Fig. 13).

Emission peaks B and G both have line emission at the same wavelength (see 2d spectrum in Figure 13). In addition component G shows extended emission, making it the source likely to be most sensitive to the photometric redshift estimate. The photometric redshift for G is $z_{BPZ} = 0.480 \pm 0.145$, from which we consider the peak ‘B+G’ as [OIII] at $z=0.532$. As it is unlikely for components B and G to have the same wavelength peak but be unrelated, we take this as the redshift for both components. The morphology of the galaxy nearest to the sources is an elliptical which is likely component G (see Fig. 12). From profile fitting we do not find associated $H\beta$. Our double-peaked spectrum (A+G) has a peak-to-peak velocity separation of $\sim 9600 \text{ km s}^{-1}$. From this remarkably-high value we can rule out the interpretation

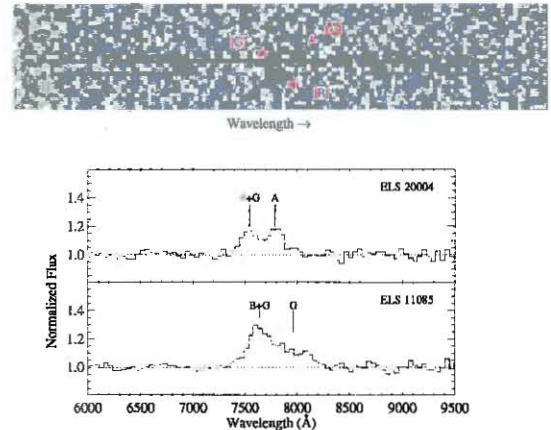


FIG. 13.— Spectra of F12.ELG2, which contain new ELSs at close angular separations: ELS 20004 ‘A,’ ELS 11085 ‘B,’ and ‘G’ (see Fig. 12 for the image). From the line placements and separations we infer there to be one emission line for each of the three components. The spectrum in the top panel is remarkable for showing a double-peaked emission line profile with a large peak-to-peak velocity difference of $\sim 9600 \text{ km s}^{-1}$, and line strengths of roughly equal amplitude. Component G shows underlying stellar continuum. Most likely A and G are at $z=0.532$ while A is at $z=0.560$, although additional data are required to confirm these line identifications for this complex system of ELSs.

of this object as two separate ELSs close in space. Most likely, G and B are both at $z=0.532$, while A is an unrelated source at $z=0.560$. It is also possible that source A and/or B are situated behind the elliptical galaxy, which would alter the above redshift identifications. Additional spectroscopy is required at a competitive spatial resolution to identify these emission features and objects.

6.2. High- z Population

We detect the highest redshift object with a published spectrum in the A1689 field, ELG 10399 at $z=5.13$ (Frye et al. 2002). Our grism spectrum is shown in the upper panel. This arclet is faint ($i_{AB} = 25.85 \pm 0.18$) and extremely red ($g - i > 4$), yet is detected in our rather shallow grism survey owing to its large rest-frame equivalent width ($W_r = 29.7^{+13.29}_{-4.6}$), its high magnification, and its small size of $1''$ (Fig. 14). We compute a magnification of $\mu \approx 4.5$, and estimate an intrinsic size for its redshift of $\approx 1 \text{ kpc}$. There are no counterarcs predicted for this arclet. We identify the lone emission line to be $\text{Ly}\alpha$ based on our higher resolution companion spectrum taken with Keck LRIS (blue dashed line) which shows also a Lyman-series break. With its high rest equivalent width of $W_r > 20$, this object would appear from the grism spectrum alone to be a $\text{Ly}\alpha$ emitter, but our Keck spectrum shows it to have a Lyman-break seen against stellar continuum.

Of the six galaxies in the field of A1689 with $z > 2.5$ (Table 4), interestingly only this one galaxy at $z=5.13$ enters into our sample. The Sextet arcs at $z=3.038$ are not detected, which is not surprising given that the arclet in this sextuply-imaged system with the strongest line emission has a $\text{Ly}\alpha$ total of $W_r = 4^{+1.5}_{-5.0} \text{ \AA}$, a value in the lowest single percentile of our sample. It is less well understood why the bright arclet at $z=4.868$ is not detected. This ar-

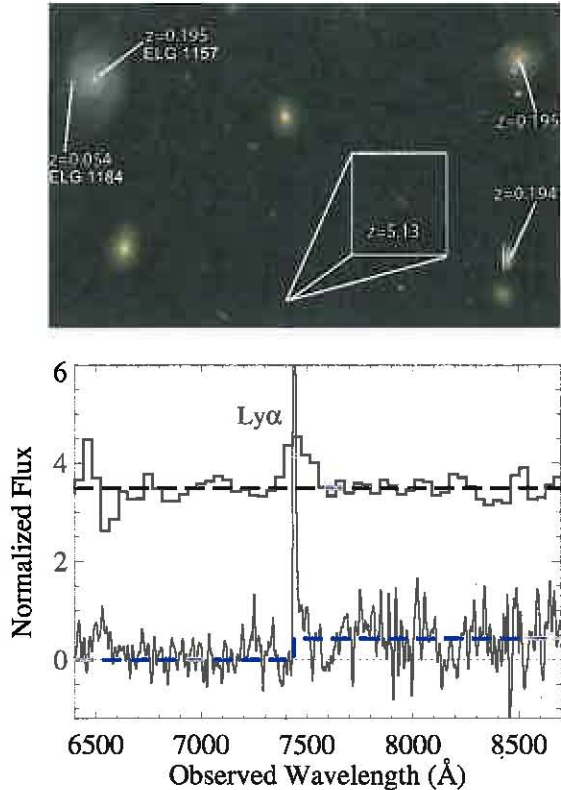


FIG. 14.— *grism* image and spectra of ELG 10399 at $z = 5.13$ ($i_{775} = 25.58 \pm 0.18$). A Lyman-series break is clearly detected together with a prominent asymmetric emission line which we take to be $\text{Ly}\alpha$ from our Keck LRIS observations (lower spectrum). Our grism results are also shown (upper spectrum). Two other ELSs from our sample appear in the field. One is ELS 1184 at $z = 0.054$ and the other is ELS 1157 at $z = 0.195$, as marked. Spectroscopic redshifts of other objects in the field known from the literature are marked.

clet image has $i_{775} = 23.48 \pm 0.03$, an angular size of $\sim 1.3''$, a $\text{Ly}\alpha$ emission line with $W_r = 12.4^{+8.83}_{-3.84}$ Å (the lowest 10% of our sample), and is situated in a relatively uncrowded location relative to the cluster members. Note we do not see any lone unassociated emission lines of other faint, potentially high-redshift objects near to the locations of the tangential critical curve.

7. SUMMARY AND FUTURE WORK

We have undertaken a census of emission line galaxies in the central portion of A1689 comprising three orbits and a single pointing with the HST ACS G800L grism. This is the first grism survey with HST in the field of a massive lensing cluster. We summarize the main results below.

- We present a spectroscopic catalog (Table 1) which contains 66 emission lines in 52 emission line sources in 43 galaxies in this flux-limited sample with $i_{775} \lesssim 27.3$. Three-fourths of the galaxy identifications are new, and one-quarter of the spectra

show a single emission line with a large rest equivalent width (~ 100 Å).

- We report the discovery of F12_ELG1 at $z=0.7895$, whose spectrum shows several Balmer emission lines indicative of a starburst phase for this young, low-mass galaxy with \sim solar metallicity and $M/L \approx 1$. Offset from the galaxy nucleus by ~ 1 kpc we measure metal line ratios that are consistent with the presence of an AGN, a result that is not apparent in the integrated spectrum. We interpret the presence of a harder ionization source outside the galaxy nucleus to be a result of shocks possibly induced by a recent galaxy interaction.
- We compute magnification factors for some individual galaxies. We construct a magnification profile for the cluster, and measure a cumulative benefit due to lensing of a factor of 3.75 within the central ≈ 500 kpc.
- We have detected the highest redshift galaxy with spectroscopic confirmation, ELG 10399 at $z=5.13$, and we report the discovery of several other objects, including F12_ELG2 with multiple sources of emission at close angular separations.

Given their high magnifications over large areas, grism surveys in the fields of massive lensing clusters are rich yet relatively unexplored territories. In particular lensing can open up the discovery space for galaxies with weak W_r emission line sources. For the typical galaxy in the background of the cluster, lensing causes both the galaxy's extended stellar continuum to be diluted and the star forming regions to be magnified but remain unresolved. This lensing effect allows the detection threshold to be lowered to include weaker W_r ELSs. The exquisite spatial resolution of HST further allows for multiple weak ELSs to be identified in each ELG. Operationally, such programs are free of lengthy selection algorithms, and so can yield rewards even with only modest investments of telescope time.

ACS was developed under NASA contract NAS 5-32865, and this research has been supported in part by NASA grant NAG5-7697 and by an equipment grant from Sun Microsystems, Inc. B. L. F. acknowledges generous hospitality at the SUNY Stony Brook Astronomy Group. D. V. B. is funded through NASA Long-Term Space Astrophysics grant NNG05GE26G. We are grateful to Sangeeta Malhotra and James Rhoads for providing useful follow-up spectroscopy on Magellan Observatories. We thank Holland Ford, Rogier Windhorst, Nicole Nesvadba, Jean-Paul Kneib and Maruša Bradač for useful discussions. Some data for this work was acquired at Keck Observatories. We also want to express our appreciation to the anonymous referee whose comments and suggestions improved the clarity of this paper. The authors wish to extend special thanks to those of Hawaiian ancestry on whose sacred mountain we are privileged to be guests. Without their generous hospitality, some of the observations presented herein would not have been possible.

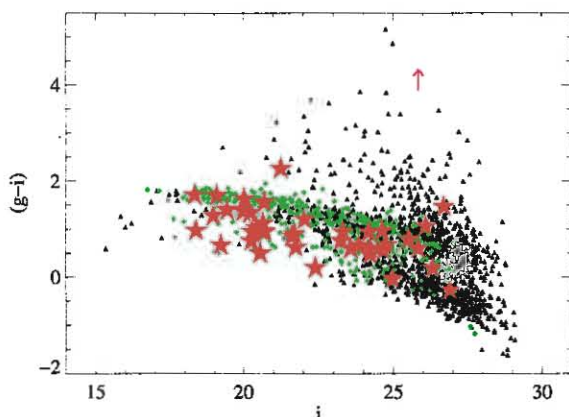


FIG. 15.— Color-magnitude diagram for HST ACS g_{475} and i_{775} in AB magnitudes. Objects in our ELG sample are indicated by the red star-shaped symbols and compared with other objects, including photometric redshifts for cluster members (green diamond shaped symbols) and photometric for all other objects (black triangular shaped symbols). The typical ELG in our sample is bluer than the cluster. The red arrow shows the lower limit in $(g-i)$ for the g -band dropout galaxy at $z=5.13$ ELG 10399.

APPENDIX THE CATALOG

In each emission line galaxy (ELG) we detect at least one emission line source (ELS) with one or more emission lines (ELs). In all we identify 66 ELs in 52 ELSs in 43 ELGs. A color-magnitude diagram of our sample is shown in Figure 15 (red star-shaped symbols), with the green diamond-shaped symbols indicating the positions of cluster members obtained by photometric redshifts. The black triangle-shaped symbols show all objects in the field with measured photometric redshifts. Most objects in our sample have colors bluer than the cluster sequence, corresponding to roughly $g-i = 1.7$ at $i_{775} = 20$. All nine $H\alpha$ Emitters (HAEs) in our sample that are cluster members are also situated below the cluster sequence. Four ELGs are situated exactly on the cluster sequence. These are not cluster members and are identified as follows: ELG 11186 (HAE at $z = 0.235$), ELG 10746 (HAE at $z = 0.230$), ELG 10226 (HAE at $z = 0.140$), and ELG 4277 (HAE at $z = 0.462$). Of these, ELG 11186 and ELG 10746 are very close to the cluster, and may be foreground galaxies experiencing infall into the cluster gravitational potential well. The three ELGs above the cluster sequence are: ELG 10399 at $z = 5.12$ with a lower limit of $g-i = 4$, the disk galaxy ELG 1077 at $z = 0.595$ with $g-i = 2.24$, and the faint and compact object ELG 6621 at $z = 0.800$ with $g-i = 1.48$.

The spectroscopic results appear in Table 1 with the following columns: object name, right ascension and declination, i_{775} (AB) magnitude, emission line central wavelength, emission line flux, total rest-frame equivalent width and $1-\sigma$ errors, line identification, spectroscopic redshift, and a reference to any redshifts in the literature determined spectroscopically. Eight line species are identified in our sample: $[S\ II]\lambda\lambda 6716, 6731$, $H\alpha$, $[O\ III]\lambda\lambda 4959, 5007$, $H\beta$, $[Ne\ III]\lambda 3367$, $He\ I\lambda 4472$, $[O\ II]\lambda\lambda 3727, 3729$, and $Ly\alpha$. The three doublets in this line list are unresolved at our spectral resolution, so we adopt the following vacuum rest wavelengths for their flux-weighted centroids: $\lambda_0([S\ II]) = 6723.5\ \text{\AA}$, $\lambda_0([O\ III]) = 4996.5\ \text{\AA}$, and $\lambda_0([O\ II]) = 3728.7\ \text{\AA}$. Two people independently measured the rest-frame equivalent widths (W_r) and found consistent results. The uncertainties reported for the line fluxes are $1-\sigma$ errors including continuum placement and photon noise. More than one-fourth of our ELGs have large rest equivalent widths, $W > 100\ \text{\AA}$.

Line Identifications

Previously published redshifts are the first resource for line identifications. For new ELGs, the objects with multiple emission lines make the redshift determination straightforward, taking into account the cases of similar ratios of wavelengths between line pairs, such as the similar line ratios of $\lambda H\alpha/\lambda [OIII]$ and $\lambda H\beta/\lambda [OII]$ (M07). The remainder of the catalog consists of single emission lines. Single ELs present challenges as grism observations are not sensitive to small-scale changes that can serve as redshift-confirming features, such as strong absorption bands and the line shape of emission lines closely-separated in velocity space. The treatment of single emission lines relies on the combination of photometric redshift, profile fitting and other sanity checks such as the search for continuum depressions and the absence of conflicting emission features. The photometric redshift is derived from a Bayesian approach, described in detail in other papers (Benítez 2000; Benítez et al. 2004; Coe et al. 2006); it is measured including nine bands and found to be a robust redshift indicator (see Fig. 9 in Frye et al. 2007). We fit profiles to distinguish secondary bumps in our single emission lines to corroborate the likelihood of, for example, a bonafide $[OIII]/H\beta$ detection. When one emission line is observed, the photometric redshift is used to resolve the degenerate possible redshift solutions, resulting in a much more accurate redshift than from the photometry alone.

The largest source of uncertainty is in establishing the goodness of fit of the zero-point of the wavelength solution. In our blind emission line finding technique, ELs are identified and the offset of the position between the emission line and the direct source are computed. The goodness of fit can be measured by comparing the grism and spectroscopic

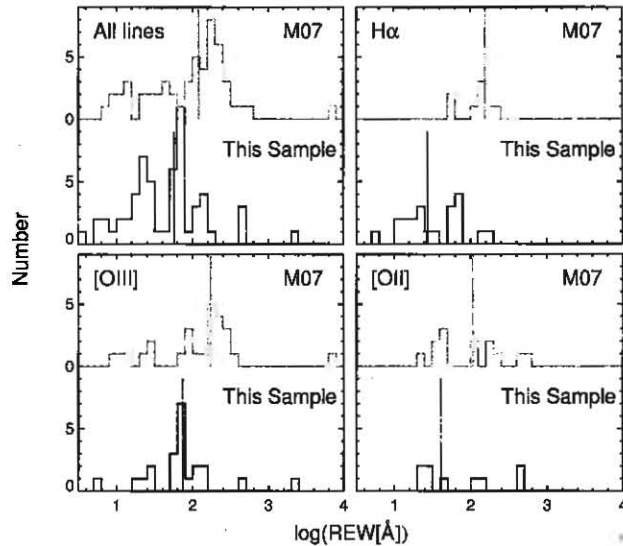


FIG. 16.— The total rest-frame equivalent width (W_r) in Angstroms of each emission line in our catalog is plotted as a histogram for all objects, and then also for the three most common line species of $H\alpha$, [OIII], and [OII]. The results for this sample appear in black in the lower row of each panel and the grism sample of the HDF-N (M07) in gray in the upper row. Our lensed sample includes more weak W_r sources of line emission. The effect of lensing is to boost the flux of the unresolved emission lines with respect to the stretched and diluted stellar continuum, thereby increasing the signal-to-noise and allowing for lower W_r detection thresholds.

redshifts. From previous studies involving similar datasets and reduction techniques as described in M07, the scatter in grism and spectroscopic redshifts is equivalent to an error in position of ~ 1 pixel, or $\Delta v = 1650 \text{ km s}^{-1}$. In addition, the spectral resolution is low, with $R=90$ at $\lambda=8500 \text{ \AA}$, corresponding to $\Delta v=3300 \text{ km s}^{-1}$ or about 2.1 pixels. While in practice this means that we will have relatively little leverage on measuring kinematics of gas clouds within a disk, the grism has the advantage of obtaining spectroscopy that is *spatially* resolved on impressively small angular scales of $\sim 0''.2$

Line Demographics

We compare line properties sorted by the three most common line species, $H\alpha$, [OIII], [OII] (Table 1), and compare these results with a recent HST ACS grism survey in an unlensed field to similar depth, the HDF grism survey (M07). By line species, $H\alpha$ emitters are plentiful despite the small sample volume owing to the field selection of a massive galaxy cluster. The median redshift for our sample of HAEs of $z = 0.22$ is close to the cluster redshift of $z = 0.187$ and is dominated by galaxies in the cluster. We measure the median W_r s to be: $W_{H\alpha} = 29.3 \text{ \AA}$, $W_{[OIII]} = 67.2 \text{ \AA}$, and $W_{[OII]} = 29.6 \text{ \AA}$. These values are large, but typical of grism surveys.

The largest difference between this sample and the HDF is in the values of the W_r . One quarter of all of the emitters in our sample have $W_r \geq 100 \text{ \AA}$, compared to three-quarters for the comparison sample (HDF-N, M07). Also, the median W_r for each line species is smaller than the values in the comparison sample (Fig. 16). The largest shift is found for the HAEs, which are dominated by galaxies in or near to this old and presumably relaxed cluster ($z=0.19$). Interestingly, all of the HAEs in our sample that are brighter than the magnitude limit of the large emission line survey of B02 of $I=19.3$ are recovered in our census. Moreover, all of the HAEs in our sample that are fainter than their limiting magnitude are new to the literature. Thus we find the slitless grism observing approach to be especially sensitive to the detection of low-luminosity (and largely unlensed) HAEs with low SFRs. On the other hand, the shift in the [OIII] and [OII] emitters towards lower W_r s is owing to lensing. Lensing boosts the brightnesses and sizes of the background objects, including the emission lines, with the effect of improving the signal to noise of the grism spectra. This effect enables the identification of weaker emission lines with smaller W_r and lower SFR than are found in the field. We compute rest-frame B -band magnitudes, M_B , by fitting a Bruzual-Charlot model to our optical ACS photometry, and then computing the k -correction onto a Johnson B -band filter template. The mean M_B for the 27 [OIII] emitters is fainter than for the HDF by 1.5 magnitudes, yielding yet another indication of the gravitational lensing effect. The shift is not seen for the 21 $H\alpha$ emitters or nine [OII] emitters which is dominated by emitters inside the cluster lens and small number statistics, respectively.

Special Cases

Seven emission lines (ELs) flagged by our purpose-built reduction code were later removed as bogus detections. In five cases the lines were weak and other available spectroscopic data ruled out the grism features as ELs. In two cases, the continuum shapes mimicked an EL but turned out to be stellar continuum. There are three cases for which the EL redshifts are not consistent with published redshifts: ELS 1184, ELS 11324, and ELG 6621. We discuss these cases below.

- ELS 1184 is in a crowded environment and is separated by only $1.8''$ from ELS 1157 (see upper left of Fig. 14). ELS 1157 has multiple emission features confirming the redshift of $z = 0.195$ for this previously identified object (Balogh et al. 2002; Duc et al. 2002). ELS 1184 has a single EL at 6917 \AA that we do not identify with any strong emission feature at or near to $z \sim 0.195$. We adopt the foreground redshift $z = 0.054$ to this compact and very bright ELS based on the absence of other expected ELs in the bandpass were the identifications to correspond to [OIII] or [OII]. We measure a photometric redshift for the Sc galaxy of $z_{BPZ} = 0.320 \pm 0.129$, but this measurement is taken at the position of ELS 1157.
- ELG 11324 is in the crowded outer regions of an extended face-on spiral galaxy with a photometric redshift of $z_{BPZ} = 0.250^{+0.260}_{-0.122}$ and a spectroscopic redshift of $z = 0.384$ (J. Richard, *private communication*). We detect a single EL at 6913.5 \AA which we take to be [OIII] at the spectroscopic redshift.
- ELG 6621 is small and faint, with a magnified size of $0'.3$ and $i_{775} = 26.7$. The grism spectrum shows a lone emission line at 6712.4 \AA with stellar continuum and no salient continuum features. This galaxy suffers from crowding by a second object that is confidently identified from our companion Magellan spectrum as ELG 6621a at $z = 0.1868$. ELG 6621a is a cluster member that is not detected in our grism dataset and that has no feature at the position of the grism EL. The photometric redshift for ELG 6621 is $z_{BPZ} = 3.780 \pm 0.468$. If the EL in ELG 6621 is Ly α then the redshift is $z=4.52$, and we cannot rule out the possibility of high redshift at least according to the redshift test available to us (Rhoads et al. 2009). The high redshift scenario would seem unlikely given that the photometry does not correct for extinction at the cluster redshift, and thus we must attribute some of its 'redness' to its being behind the foreground cluster member. Strictly, the EL can be also H α , [OII] or [OIII]. If the line is [OIII] then $z=0.346$, in which case we do not detect the non-requisite H β EL. Based on the large observed equivalent width of 772.9 ± 497.9 we adopt a line identification of [OII] at $z = 0.800$, and admit this as an uncertain redshift in our sample. Note ELG 6621a is detected only in our Magellan spectrum and so does not appear in Table 1.

REFERENCES

- Allende Prieto, C., Lambert, D. L., & Asplund, M. 2002, ApJ, 573, L137
- Asplund, M., Grevesse, N., Sauval, A. J., Allende Prieto, C., & Kiselman, D. 2004, A&A, 417, 751
- Atek, H., Siana, B., Scarlata, C., Malkan, M., McCarthy, P., Teplitz, H., Henry, A., Colbert, J., Bridge, C., Bunker, A. J., Dressler, A., Fosbury, R., Hathi, N. P., Martin, C., Ross, N. R., & Shim, H. 2011, ArXiv e-prints
- Baldwin, J. A., Phillips, M. M., & Terlevich, R. 1981, PASP, 93, 5
- Balogh, M. L., Couch, W. J., Smail, I., Bower, R. G., & Glazebrook, K. 2002, MNRAS, 335, 10
- Balogh, M. L., Morris, S. L., Yee, H. K. C., Carlberg, R. G., & Ellingson, E. 1999, ApJ, 527, 54
- Bauer, A. E., Drory, N., Hill, G. J., & Feulner, G. 2005, ApJ, 621, L89
- Benítez, N. 2000, ApJ, 536, 571
- Benítez, N., Ford, H., Bouwens, R., Menanteau, F., Blakeslee, J., Gronwall, C., Illingworth, G., Meurer, G., Broadhurst, T. J., Clampin, M., Franx, M., Hartig, G. F., Magee, D., Sirianni, M., Ardila, D. R., Bartko, F., Brown, R. A., Burrows, C. J., Cheng, E. S., Cross, N. J. G., Feldman, P. D., Golimowski, D. A., Infante, L., Kimble, R. A., Krist, J. E., Lesser, M. P., Levay, Z., Martel, A. R., Miley, G. K., Postman, M., Rosati, P., Sparks, W. B., Tran, H. D., Tsvetanov, Z. I., White, R. L., & Zheng, W. 2004, ApJS, 150, 1
- Bertin, E., & Arnouts, S. 1996, A&AS, 117, 393
- Blakeslee, J. P., Anderson, K. R., Meurer, G. R., Benítez, N., & Magee, D. 2003, in Astronomical Society of the Pacific Conference Series, Vol. 295, Astronomical Data Analysis Software and Systems XII, ed. H. E. Payne, R. I. Jedrzejewski, & R. N. Hook, 257
- Brinchmann, J., Pettini, M., & Charlot, S. 2008, MNRAS, 385, 769
- Broadhurst, T., Benítez, N., Coe, D., Sharon, K., Zekser, K., White, R., Ford, H., Bouwens, R., Blakeslee, J., Clampin, M., Cross, N., Franx, M., Frye, B., Hartig, G., Illingworth, G., Infante, L., Menanteau, F., Meurer, G., Postman, M., Ardila, D. R., Bartko, F., Brown, R. A., Burrows, C. J., Cheng, E. S., Feldman, P. D., Golimowski, D. A., Goto, T., Gronwall, C., Herranz, D., Holden, B., Homeier, N., Krist, J. E., Lesser, M. P., Martel, A. R., Miley, G. K., Rosati, P., Sirianni, M., Sparks, W. B., Steindling, S., Tran, H. D., Tsvetanov, Z. I., & Zheng, W. 2005, ApJ, 621, 53
- Bruzual, G., & Charlot, S. 2003, MNRAS, 344, 1000
- Calzetti, D., Armus, L., Bohlin, R. C., Kinney, A. L., Koornneef, J., & Storchi-Bergmann, T. 2000, ApJ, 533, 682
- Charlot, S., & Longhetti, M. 2001, MNRAS, 323, 887
- Coe, D., Benítez, N., Broadhurst, T., & Moustakas, L. A. 2010, ApJ, 723, 1678
- Coe, D., Benítez, N., Sánchez, S. F., Jee, M., Bouwens, R., & Ford, H. 2006, AJ, 132, 926
- Conselice, C. J., Bluck, A. F. L., Buitrago, F., Bauer, A. E., Grützbauch, R., Bouwens, R. J., Bevan, S., Mortlock, A., Dickinson, M., Daddi, E., Yan, H., Scott, D., Chapman, S. C., Chary, R.-R., Ferguson, H. C., Gialavisco, M., Grogin, N., Illingworth, G., Jogee, S., Koekemoer, A. M., Lucas, R. A., Mobasher, B., Moustakas, L., Papovich, C., Ravindranath, S., Siana, B., Teplitz, H., Trujillo, I., Urry, M., & Weinzierl, T. 2011, MNRAS, 413, 80
- Damen, M., Labbé, I., Franx, M., van Dokkum, P. G., Taylor, E. N., & Gawiser, E. J. 2009, ApJ, 690, 937
- Duc, P.-A., Poggianti, B. M., Fadda, D., Elbaz, D., Flores, H., Chianal, P., Franceschini, A., Moorwood, A., & Cesarsky, C. 2002, A&A, 382, 60
- Elbaz, D., Daddi, E., Le Borgne, D., Dickinson, M., Alexander, D. M., Chary, R.-R., Starck, J.-L., Brandt, W. N., Kitzbichler, M., MacDonald, E., Nonino, M., Popesso, P., Stern, D., & Vanzella, E. 2007, A&A, 468, 33
- Erb, D. K., Shapley, A. E., Pettini, M., Steidel, C. C., Reddy, N. A., & Adelberger, K. L. 2006, ApJ, 644, 813

- Faber, S. M., Phillips, A. C., Kibrick, R. I., Alcott, B., Allen, S. L., Burrous, J., Cantrall, T., Clarke, D., Coil, A. L., Cowley, D. J., Davis, M., Deich, W. T. S., Dietsch, K., Gilmore, D. K., Harper, C. A., Hilyard, D. F., Lewis, J. P., McVeigh, M., Newman, J., Osborne, J., Schiavon, R., Stover, R. J., Tucker, D., Wallace, V., Wei, M., Wirth, G., & Wright, C. A. 2003, in *Society of Photo-Optical Instrumentation Engineers (SPIE) Conference Series*, Vol. 4841, *Society of Photo-Optical Instrumentation Engineers (SPIE) Conference Series*, ed. M. Iye & A. F. M. Moorwood, 1657–1669
- Ferreras, I., Pasquali, A., Malhotra, S., Rhoads, J., Cohen, S., Windhorst, R., Pirzkal, N., Grogin, N., Koekemoer, A. M., Lisker, T., Panagia, N., Daddi, E., & Hathi, N. P. 2009, *ApJ*, 706, 158
- Feulner, G., Gabasch, A., Salvato, M., Drory, N., Hopp, U., & Bender, R. 2005, *ApJ*, 633, L9
- Frye, B., Broadhurst, T., & Benítez, N. 2002, *ApJ*, 568, 558
- Frye, B. L., Bowen, D. V., Hurley, M., Tripp, T. M., Fan, X., Holden, B., Guhathakurta, P., Coe, D., Broadhurst, T., Egami, E., & Meylan, G. 2008, *ApJ*, 685, L5
- Frye, B. L., Coe, D., Bowen, D. V., Benítez, N., Broadhurst, T., Guhathakurta, P., Illingworth, G., Menanteau, F., Sharon, K., Lup-ton, R., Meylan, G., Zekser, K., Meurer, G., & Hurley, M. 2007, *ApJ*, 665, 921
- González Delgado, R. M., Leitherer, C., & Heckman, T. M. 1999, *ApJS*, 125, 489
- Grogin, N. A., Kocevski, D. D., Faber, S. M., Ferguson, H. C., Koekemoer, A. M., Riess, A. G., Acquaviva, V., Alexander, D. M., Almaini, O., Ashby, M. L. N., Barden, M., Bell, E. F., Bournaud, F., Brown, T. M., Caputi, K. I., Casertano, S., Cassata, P., Castellano, M., Challis, P., Chary, R.-R., Cheung, E., Cirasuolo, M., Conselice, C. J., Roshan Cooray, A., Croton, D. J., Daddi, E., Dahlen, T., Davé, R., de Mello, D. F., Dekel, A., Dickinson, M., Dolch, T., Donley, J. L., Dunlop, J. S., Dutton, A. A., Elbaz, D., Fazio, G. G., Filippenko, A. V., Finkelstein, S. L., Fontana, A., Gardner, J. P., Garnavich, P. M., Gawiser, E., Giavalisco, M., Grazian, A., Guo, Y., Hathi, N. P., Häussler, B., Hopkins, P. F., Huang, J.-S., Huang, K.-H., Jha, S. W., Kartaltepe, J. S., Kirshner, R. P., Koo, D. C., Lai, K., Lee, K.-S., Li, W., Lotz, J. M., Lucas, R. A., Madau, P., McCarthy, P. J., McGrath, E. J., McIntosh, D. H., McLure, R. J., Mobasher, B., Moustakas, L. A., Mozena, M., Nandra, K., Newman, J. A., Niemi, S.-M., Noeske, K. G., Papovich, C. J., Pentericci, L., Pope, A., Primack, J. R., Rajan, A., Ravindranath, S., Reddy, N. A., Rix, H.-W., Robaina, A. R., Rosario, D. J., Rosati, P., Salimbeni, S., Scarlata, C., Siana, B., Simard, L., Smidt, J., Snyder, D., Somerville, R. S., Spinrad, H., Straughn, A. N., Telford, O., Teplitz, H. I., Trump, J. R., Vargas, C., Villforth, C., Wagner, C. R., Wandro, P., Wechsler, R. H., Weiner, B. J., Wiklind, T., Wild, V., Wilson, G., Wuyts, S., & Yun, M. S. 2011, *ApJS*, 197, 36
- Kriek, M., van Dokkum, P. G., Franx, M., Illingworth, G. D., & Magee, D. K. 2009, *ApJ*, 705, L71
- Kümmel, M., Walsh, J. R., Pirzkal, N., Kuntschner, H., & Pasquali, A. 2009, *PASP*, 121, 59
- Lamareille, F. 2010, *A&A*, 509, A53+
- Lamareille, F., Brinchmann, J., Contini, T., Walcher, C. J., Charlot, S., Pérez-Montero, E., Zamorani, G., Pozzetti, L., Bolzonella, M., Garilli, B., Paltani, S., Bongiorno, A., Le Fèvre, O., Bottini, D., Le Brun, V., Maccagni, D., Scaramella, R., Scodreggio, M., Tresse, L., Vettolani, G., Zanichelli, A., Adami, C., Arnouts, S., Bardelli, S., Cappi, A., Ciliegi, P., Foucaud, S., Franzetti, P., Gavignaud, I., Guzzo, L., Ibert, O., Iovino, A., McCracken, H. J., Marano, B., Marinoni, C., Mazure, A., Meneux, B., Merighi, R., Pellò, R., Pollo, A., Radovich, M., Vergani, D., Zucca, E., Romano, A., Grado, A., & Limatola, L. 2009, *A&A*, 495, 53
- Lamareille, F., Contini, T., Brinchmann, J., Le Borgne, J.-F., Charlot, S., & Richard, J. 2006, *A&A*, 448, 907
- Lamareille, F., Mouchine, M., Contini, T., Lewis, I., & Maddox, S. 2004, *MNRAS*, 350, 396
- Lehnert, M. D., Nesvadba, N. P. H., Le Tiran, L., Di Matteo, P., van Driel, W., Douglas, L. S., Chemin, L., & Bournaud, F. 2009, *ApJ*, 699, 1660
- Leonard, A., Goldberg, D. M., Haaga, J. L., & Massey, R. 2007, *ArXiv Astrophysics e-prints*
- Lilly, S. J., Le Fèvre, O., Hammer, F., & Crampton, D. 1996, *ApJ*, 460, L1
- Limousin, M., Richard, J., Jullo, E., Kneib, J.-P., Fort, B., Soucail, G., Elfasdóttir, Á., Natarajan, P., Ellis, R. S., Smail, I., Czoske, O., Smith, G. P., Hudelot, P., Bardeau, S., Ebeling, H., Egami, E., & Knudsen, K. K. 2007, *ApJ*, 668, 643
- Liu, X., Shapley, A. E., Coil, A. L., Brinchmann, J., & Ma, C.-P. 2008, *ApJ*, 678, 758
- Malhotra, S., Rhoads, J. E., Pirzkal, N., Haiman, Z., Xu, C., Daddi, E., Yan, H., Bergeron, L. E., Wang, J., Ferguson, H. C., Gronwall, C., Koekemoer, A., Kuemmel, M., Moustakas, L. A., Panagia, N., Pasquali, A., Stiavelli, M., Walsh, J., Windhorst, R. A., & di Serego Alighieri, S. 2005, *ApJ*, 626, 666
- Marocco, J., Hache, E., & Lamareille, F. 2011, *A&A*, 531, A71
- McGaugh, S. S. 1991, *ApJ*, 380, 140
- Meurer, G. R., Tsvetanov, Z. I., Gronwall, C., Capak, P., Blakeslee, J. P., Benítez, N., Ford, H. C., Illingworth, G. D., Bradley, L. D., Pirzkal, N., Walsh, J., Bouwens, R. J., & Srinivasan, S. 2007, *AJ*, 134, 77
- Nagao, T., Maiolino, R., & Marconi, A. 2006, *A&A*, 459, 85

- Nilsson, K. K., Möller-Nilsson, O., Rosati, P., Lombardi, M., Kümmel, M., Kuntschner, H., Walsh, J. R., & Fosbury, R. A. E. 2011, *A&A*, 526, A10
- Osterbrock, D. 1989, *The Astrophysics of Gaseous Nebulae and Active Galactic Nuclei* (Mill Valley: Univ. Science Books)
- Pérez-Montero, E., Contini, T., Lamareille, F., Brinchmann, J., Walcher, C. J., Charlot, S., Bolzonella, M., Pozzetti, L., Bottini, D., Garilli, B., Le Brun, V., Le Fèvre, O., Maccagni, D., Scaramella, R., Scoddeggio, M., Tresse, L., Vettolani, G., Zanichelli, A., Adami, C., Arnouts, S., Bardelli, S., Cappi, A., Ciliegi, P., Foucaud, S., Franzetti, P., Gavignaud, I., Guzzo, L., Ilbert, O., Iovino, A., McCracken, H. J., Marano, B., Marinoni, C., Mazure, A., Meneux, B., Merighi, R., Paltani, S., Pellò, R., Pollo, A., Radovich, M., Vergani, D., Zamorani, G., & Zucca, E. 2009, *A&A*, 495, 73
- Queyrel, J., Contini, T., Kissler-Patig, M., Epinat, B., Amram, P., Garilli, B., Le Fèvre, O., Moutaka, J., Paicor, L., Tasca, L., Tresse, L., Vergani, D., Lopez-Sanjuan, C., & Perez-Montero, E. 2011, *ArXiv e-prints*
- Reddy, N. A., Erb, D. K., Steidel, C. C., Shapley, A. E., Adelberger, K. L., & Pettini, M. 2005, *ApJ*, 633, 748
- Reddy, N. A., Steidel, C. C., Pettini, M., Adelberger, K. L., Shapley, A. E., Erb, D. K., & Dickinson, M. 2008, *ApJS*, 175, 48
- Rhoads, J. E., Malhotra, S., Pirzkal, N., Dickinson, M., Cohen, S., Grogin, N., Hathi, N., Xu, C., Ferreras, I., Gronwall, C., Koekemoer, A., Kümmel, M., Meurer, G., Panagia, N., Pasquali, A., Ryan, R., Straughn, A., Walsh, J., Windhorst, R. A., & Yan, H. 2009, *ApJ*, 697, 942
- Richard, J., Jones, T., Ellis, R., Stark, D. P., Livermore, R., & Swinbank, M. 2011, *MNRAS*, 413, 643
- Rigby, J. R., Wuyts, E., Gladders, M. D., Sharon, K., & Becker, G. D. 2011, *ApJ*, 732, 59
- Rodighiero, G., Cimatti, A., Gruppioni, C., Popesso, P., Andreani, P., Altieri, B., Aussel, H., Berta, S., Bongiovanni, A., Brisbin, D., Cava, A., Cepa, J., Daddi, E., Dominguez-Sanchez, H., Elbaz, D., Fontana, A., Förster Schreiber, N., Franceschini, A., Genzel, R., Grazian, A., Lutz, D., Magdis, G., Magliocchetti, M., Magnelli, B., Maiolino, R., Mancini, C., Norcon, R., Perez Garcia, A. M., Poglitsch, A., Santini, P., Sanchez-Portal, M., Pozzi, F., Riguccini, L., Saintonge, A., Shao, L., Sturm, E., Tacconi, L., Valtchanov, I., Wetzstein, M., & Wierprecht, E. 2010, *A&A*, 518, L25
- Rola, C. S., Terlevich, E., & Terlevich, R. J. 1997, *MNRAS*, 289, 419
- Somerville, R. S. 2009, *MNRAS*, 399, 1988
- Straughn, A. N., Kuntschner, H., Kümmel, M., Walsh, J. R., Cohen, S. H., Gardner, J. P., Windhorst, R. A., O'Connell, R. W., Pirzkal, N., Meurer, G., McCarthy, P. J., Hathi, N. P., Malhotra, S., Rhoads, J., Balick, B., Bond, H. E., Calzetti, D., Disney, M. J., Dopita, M. A., Frogel, J. A., Hall, D. N. B., Holtzman, J. A., Kimble, R. A., Mutchler, M., Paresce, F., Saha, A., Silk, J. I., Trauger, J. T., Walker, A. R., Whitmore, B. C., Young, E. T., & Xu, C. 2011, *AJ*, 141, 14
- Straughn, A. N., Meurer, G. R., Pirzkal, N., Cohen, S. H., Malhotra, S., Rhoads, J., Windhorst, R. A., Gardner, J. P., Hathi, N. P., Xu, C., Gronwall, C., Koekemoer, A. M., Walsh, J., & di Serego Alighieri, S. 2008, *AJ*, 135, 1624
- Straughn, A. N., Pirzkal, N., Meurer, G. R., Cohen, S. H., Windhorst, R. A., Malhotra, S., Rhoads, J., Gardner, J. P., Hathi, N. P., Jansen, R. A., Grogin, N., Panagia, N., di Serego Alighieri, S., Gronwall, C., Walsh, J., Pasquali, A., & Xu, C. 2009, *AJ*, 138, 1022
- Tremonti, C. A., Heckman, T. M., Kauffmann, G., Brinchmann, J., Charlot, S., White, S. D. M., Seibert, M., Peng, E. W., Schlegel, D. J., Uomoto, A., Fukugita, M., & Brinkmann, J. 2004, *ApJ*, 613, 898
- Trump, J. R., Weiner, B. J., Scarlata, C., Kocevski, D. D., Bell, E. F., McGrath, E. J., Koo, D. C., Faber, S. M., Laird, E. S., Mozena, M., Rangel, C., Yan, R., Yesuf, H., Atek, H., Dickinson, M., Donley, J. L., Dunlop, J. S., Ferguson, H. C., Finkelstein, S. L., Grogin, N. A., Hathi, N. P., Juneau, S., Kartaltepe, J. S., Koekemoer, A. M., Nandra, K., Newman, J. A., Rodney, S. A., Straughn, A. N., & Teplitz, H. I. 2011, *ApJ*, 743, 144
- van der Wel, A., Franx, M., van Dokkum, P. G., Rix, H.-W., Illingworth, G. D., & Rosati, P. 2005, *ApJ*, 631, 145
- van der Wel, A., Straughn, A. N., Rix, H.-W., Finkelstein, S. L., Koekemoer, A. M., Weiner, B. J., Wuyts, S., Bell, E. F., Faber, S. M., Trump, J. R., Koo, D. C., Ferguson, H. C., Scarlata, C., Hathi, N. P., Dunlop, J. S., Newman, J. A., Dickinson, M., Jahnke, K., Salmon, B. W., de Mello, D. F., Kocevski, D. D., Lai, K., Grogin, N. A., Rodney, S. A., Guo, Y., McGrath, E. J., Lee, K.-S., Barro, G., Huang, K.-H., Riess, A. G., Ashby, M. L. N., & Willner, S. P. 2011, *ApJ*, 742, 111
- Windhorst, R. A., Cohen, S. H., Hathi, N. P., McCarthy, P. J., Ryan, Jr., R. E., Yan, H., Baldry, I. K., Driver, S. P., Frogel, J. A., Hill, D. T., Kelvin, L. S., Koekemoer, A. M., Mechtley, M., O'Connell, R. W., Robotham, A. S. G., Rutkowski, M. J., Seibert, M., Straughn, A. N., Tuffs, R. J., Balick, B., Bond, H. E., Bushouse, H., Calzetti, D., Crockett, M., Disney, M. J., Dopita, M. A., Hall, D. N. B., Holtzman, J. A., Kaviraj, S., Kimble, R. A., MacKenty, J. W., Mutchler, M., Paresce, F., Saha, A., Silk, J. I., Trauger, J. T., Walker, A. R., Whitmore, B. C., & Young, E. T. 2011, *ApJS*, 193, 27
- Wright, S. A., Larkin, J. E., Graham, J. R., & Ma, C.-P. 2010, *ApJ*, 711, 1291
- Xia, L., Malhotra, S., Rhoads, J., Pirzkal, N., Zheng, Z., Meurer, G., Straughn, A., Grogin, N., & Floyd, D. 2011, *AJ*, 141, 64
- Xu, C., Pirzkal, N., Malhotra, S., Rhoads, J. E., Mobasher, B., Daddi, E., Gronwall, C., Hathi, N. P., Panagia, N., Ferguson, H. C., Koekemoer, A. M., Kümmel, M., Moustakas, L. A., Pasquali, A., di Serego Alighieri, S., Vernet, J., Walsh, J. R., Windhorst, R., & Yan, H. 2007, *AJ*, 134, 169
- Yuan, T., & Kewley, L. J. 2009, *ApJ*, 699, L161
- Zaritsky, D., Kennicutt, Jr., R. C., & Huchra, J. P. 1994, *ApJ*, 420, 87
- Zekser, K. C., White, R. L., Broadhurst, T. J., Benítez, N., Ford, H. C., Illingworth, G. D., Blakeslee, J. P., Postman, M., Jee, M. J., & Coe, D. A. 2006, *ApJ*, 640, 639
- Zheng, X. Z., Bell, E. F., Papovich, C., Wolf, C., Meisenheimer, K., Rix, H.-W., Rieke, G. H., & Somerville, R. 2007, *ApJ*, 661, L41

TABLE 1
SPECTROSCOPIC CATALOG OF GALAXIES IN THE FIELD OF A1689

ID	RA (hours)	DEC ($^{\circ}$)	z_{775} (AB)	Line Center (\AA)	$\log(fI)$ ($\text{erg s}^{-1} \text{cm}^{-2}$)	REW (\AA)	Line ID	$z_{g,rism}$	Ref
6621	13.189628	-1.3506333	26.69 ± 0.04	6712.4	-16.63	429 ± 277	[OII]	0.800	
3483	13.189729	-1.323381	20.11 ± 0.01	8921.4	-15.25	—	HeI	0.04	
11260	13.190046	-1.348567	24.21 ± 0.01	9010.5	-15.74	2034.8 ± 483.0	[OIII]	0.810	
6381	13.190094	-1.341133	24.17 ± 0.01	8740.6	-16.06	97.2 ± 19.5	[OIII]	0.758	
11186	13.190131	-1.353053	18.33 ± 0.01	8126.7	-15.86	6.1 ± 1.4	H α	0.235	a
11136	13.190185	-1.357363	23.32 ± 0.01	8045.1	-16.35	65.8 ± 15.2	[OIII]	0.615	
11322	13.190542	-1.326375	19.82 ± 0.01	9505.6	-16.18	67.5 ± 16.1	H α	0.449	a
6182	13.190737	-1.324731	24.66 ± 0.01	8383.4	-16.54	59.4 ± 20.0	H α	0.277	
11226	13.190740	-1.3298028	21.61 ± 0.01	7783.1	-16.61	13.3 ± 5.0	H α	0.186	
11040	13.190872	-1.349414	18.97 ± 0.01	7983.6	-16.09	10.7 ± 2.7	H α	0.215	a, b
4752	13.190875	-1.3495417	18.97 ± 0.01	7956.9	-16.06	10.8 ± 1.3	H α	0.212	a, b
6680	13.190824	-1.311189	25.83 ± 0.03	7332.8	-16.59	< 87	[OIII]	0.470	
5582	13.190834	-1.334439	26.32 ± 0.04	7531.3	-16.42	66.3 ± 17.9	[OIII]	0.510	
11324	13.190896	-1.313931	21.70 ± 0.01	6913.5	-16.55	54.6 ± 15.1	[OIII]	0.384	c
4971	13.190906	-1.349731	18.97 ± 0.01	7972.9	-15.89	64.1 ± 8.7	H α	0.202	a, b
6583	13.190941	-1.309417	23.84 ± 0.01	7932.0	-16.69	< 50	[OIII]	0.590	
6578	13.190947	-1.309414	23.84 ± 0.01	7917.2	-16.19	< 137	[OIII]	0.590	
4277	13.191041	-1.352267	20.70 ± 0.01	9571.7	-15.62	18.3 ± 1.7	H α	0.462	
4298	13.191076	-1.351167	21.74 ± 0.01	7933.4	-15.74	70.4 ± 5.5	H α	0.209	
"	"	"	"	6012.6	-15.77	17.5 ± 2.2	[OIII]	"	
"	"	"	"	8128.4	-16.20	18.1 ± 2.6	[SII]	"	
4251	13.191098	-1.350869	21.74 ± 0.01	7978.2	-16.21	57.8 ± 12.1	H α	0.210	
5700	13.191123	-1.321883	22.04 ± 0.01	7966.7	-15.57	107.3 ± 6.0	[OII]	1.139	c
"	"	"	"	8235.6	-16.41	24.3 ± 3.6	[NeIII]	"	
5570	13.191162	-1.323636	23.57 ± 0.01	8155.7	-16.19	73.4 ± 16.4	[OIII]	0.637	
11149	13.191176	-1.323664	23.57 ± 0.01	8115.4	-16.23	144.2 ± 42.4	[OIII]	0.629	
6154	13.191220	-1.309083	23.24 ± 0.01	7344.0	-16.31	127.2 ± 21.9	[OIII]	0.473	a
4744	13.191277	-1.338045	24.73 ± 0.02	8826.7	-15.74	149.3 ± 11.6	[OII]	1.368	
10640 ^a	13.191326	-1.361966	20.56 ± 0.01	6656.1	-16.05	41.2 ± 6.6	[OII]	0.783	a, d
"	"	"	"	8928.1	-16.24	74.5 ± 19.3	[OIII]	0.787	
10638 ^a	13.191334	-1.362022	"	6753.2	-16.16	26.1 ± 5.0	[OII]	0.820	a, d
"	"	"	"	9020.8	-16.27	77.5 ± 7.7	[OIII]	0.807	
20002 ^a	13.191347	-1.362072	"	6673.2	-16.31	24.1 ± 4.1	[OII]	0.790	a, d
"	"	"	"	8935.5	-15.98	77.8 ± 9.8	[OIII]	"	
2630	13.191381	-1.363211	24.97 ± 0.02	6658.2	-16.44	104.3 ± 26.8	[OIII]	0.335	
2494	13.191546	-1.360030	24.21 ± 0.01	6071.8	-15.86	407.9 ± 66.3	[OIII]	0.215	
"	"	"	"	7970.2	-16.35	176.3 ± 45.9	H α	"	
10746	13.191596	-1.350106	19.08 ± 0.01	8069.4	-16.09	21.2 ± 3.2	H α	0.230	
11085	13.191659	-1.317806	20.43 ± 0.01	7652.2	-15.68	61.4 ± 4.2	[OIII]	0.532	
20004	13.191663	-1.317805	20.43 ± 0.01	7790.0	-16.15	28.4 ± 1.7	[OIII]	0.560	
"	"	"	20.43 ± 0.01	7560.1	-15.86	29.3 ± 2.3	[OIII]	0.513	
5158	13.191787	-1.313802	24.62 ± 0.01	8332.8	-15.67	< 296	[OIII]	0.671	
"	"	"	"	8123.4	-16.80	...	H β	"	
1946	13.191900	-1.360658	20.57 ± 0.01	8419.0	-15.71	78.5 ± 12.1	[OIII]	0.700	a, e
"	"	"	"	6352.2	-16.05	20.7 ± 4.7	[OII]	"	
4194	13.191980	-1.323292	22.40 ± 0.01	8001.5	-16.31	29.1 ± 7.1	[OII]	1.145	c
10412	13.192066	-1.359247	20.65 ± 0.01	7736.1	-15.87	34.5 ± 8.0	H α	0.179	
10782	13.192252	-1.326700	19.22 ± 0.01	7566.0	-15.88	27.6 ± 2.4	H α	0.153	b
3203	13.192258	-1.326697	19.22 ± 0.01	7678.8	-15.26	72.4 ± 3.3	H α	0.170	b
"	"	"	"	7866.8	-16.21	7.1 ± 1.0	[SII]	"	
10154	13.192360	-1.371497	20.26 ± 0.01	6715.2	-16.00	59.5 ± 9.2	[OIII]	0.115	a
10226	13.192504	-1.361381	20.02 ± 0.01	7479.4	-16.60	19.7 ± 7.1	H α	0.140	
1651	13.192538	-1.3473694	25.51 ± 0.02	8850.5	-15.94	434.2 ± 114.0	[OII]	1.38	
804	13.193044	-1.351555	26.91 ± 0.07	6588.0	-16.56	106.1 ± 33.6	[OIII]	0.320	
10399	13.193055	-1.330869	25.85 ± 0.02	7445.9	-16.63	< 100	Ly α	5.13	e, f
1077	13.193131	-1.341633	21.25 ± 0.01	7967.6	-16.17	23.2 ± 2.8	[OIII]	0.595	a, e
1184	13.193212	-1.337078	18.37 ± 0.01	6917.1	-15.42	61.3 ± 5.5	H α	0.054	a, b
1157	13.193232	-1.336661	18.37 ± 0.01	7852.0	-14.82	133.6 ± 6.0	H α	0.195	a, b
"	"	"	"	5970.9	-15.78	5.5 ± 1.1	[OIII]	"	
"	"	"	"	5795.5	-15.53	3.5 ± 1.3	H β	"	
"	"	"	"	7040.1	-15.94	8.6 ± 2.1	HeI	"	
1507	13.193252	-1.326861	20.22 ± 0.01	7833.0	-16.37	15.7 ± 3.3	H α	0.194	
1094	13.193518	-1.328469	19.44 ± 0.01	7848.0	-15.89	23.7 ± 2.2	H α	0.195	b
"	"	"	"	8035.6	-16.38	6.7 ± 1.2	[SII]	"	
486	13.193702	-1.335958	26.08 ± 0.03	8057.7	-16.57	< 92	[OIII]	0.615	
20001	13.193894	-1.335958	20.28 ± 0.01	7901.7	-16.11	20.2 ± 2.2	H α	0.205	b

^a Spectroscopic redshift from the catalog of Duc et al. (2002)

^b Spectroscopic redshift from the catalog of Balogh et al. (2002)

^c Spectroscopic redshift from Richard et al. 2008, private communication.

^d This is an emission line in the ELG F12.ELG1.

^e Spectroscopic redshift from the of Frye et al. (2007)

^f Spectroscopic redshift from the catalog of Frye et al. (2002)

TABLE 2
ELGs WITH MULTIPLE EMISSION
LINE SOURCES

Group	ID	z_{ELS}
1 ^a	10782	0.153
	3203	0.170
2 (F12_ELG2)	20004	0.560
	11085	0.532
3	4971	0.202
	4752	0.212
	11040	0.215
4 ^b	4298	0.209
	4251	0.210
5	6583	0.590
	6578	0.590
6	11149	0.629
	5570	0.637
	10638 "B"	0.815
7 (F12_ELG1)	20002 "A"	0.790
	10640 "C"	0.785

^a ELS 10782 is in the foreground of A1689.

^b There is a third ELS projected near to the line of sight but with different colors, ELS 4277 at $z_{grism} = 0.462$.

TABLE 3
INTRINSIC FLUXES FOR
F12_ELG1

Line	Line Flux ^a (ergs s ⁻¹ cm ⁻²)
[O II]	$1.2^{+0.34}_{-0.27} \times 10^{-15}$
[O III] ^b	$1.8^{+0.17}_{-0.32} \times 10^{-15}$
[Ne III]	$6.0^{+0.12}_{-4.2} \times 10^{-17}$
H β ^c	$3.0^{+1.1}_{-1.2} \times 10^{-16}$
H γ ^c	$1.0^{+1.0}_{-0.88} \times 10^{-16}$

^a Line fluxes are measured from the Keck spectroscopy and are corrected for extinction and cluster magnification.

^b [O III] λ 4959 is contaminated by night sky lines, so we adopt the line ratio [O II] λ 4959, 5007 = 1.3 \times [O III] λ 5007. The flux value is taken from the Gaussian fit to the line.

^c Balmer line fluxes are additionally corrected for underlying stellar absorption.

TABLE 4
OBJECTS WITH SPECTROSCOPY AT $z > 2.5$ IN THE A1689 FIELD

RA (hours)	DEC ($^{\circ}$)	Redshift	Image Size ^a (")	Intrinsic Size ^b (h^{-1} kpc)	i_{775} (AB)	$W_{Ly\alpha}$ (\AA)	Ref
13.190701	-1.3320694	3.038	1.3	0.08	23.07 ± 0.01	$4.0^{+1.5}_{-5.0}$	c, d
13.190681	-1.3324306	3.038	2.2	1.1	22.40 ± 0.01	$-26^{+1.7}_{-1.5}$	c, d
13.192517	-1.3409444	3.038	0.75	0.73	24.02 ± 0.01	$-4.0^{+1.5}_{-11.5}$	c, d
13.191649	-1.3207361	3.770	2.3	0.22	24.13 ± 0.90	≤ 3.3	d, e
13.190402	-1.3477333	4.868	1.3	0.13	23.48 ± 0.03	$12.4^{+8.83}_{-3.84}$	d, e, f
13.193053	-1.3308528	5.120	0.64	~ 1	25.58 ± 0.18	$29.7^{+13.29}_{-4.6}$	d, e, g

^a Image size is measured from the HST ACS i_{775} image directly, without applying a lensing correction factor.

^b Linear size is computed from the image size, given a lensing magnification factor and our adopted cosmology.

^c Broadhurst et al. (2005)

^d Frye et al. (2007)

^e Frye et al. (2002)

^f Frye et al. (2008)

^g This paper.

TABLE 5
 PROPERTIES OF ELSS BY LINE SPECIES

	H α	[OIII]	[OII]
Number ELSS	21 ^a	27 ^b	9 ^c
Mean z	0.22	0.51	0.92
Mean M_B	-18.1	-18.6	-20.8
Mean W_r ^d (Å)	40.4	170	137

^a There are 18 ELGs that are H α emitters.

^b There are 22 ELGs that are [OIII] emitters.

^c There are 7 ELGs that are [OII] emitters.

^d Given large uncertainties in the background subtraction, we report W_r s for only 23 [OIII] emitters.